Wave Breaking Dissipation in a Fetch-Limited Sea

Michael Schwendeman

A thesis
submitted in partial fulfillment of the
requirements for the degree of

Master of Science in Engineering

University of Washington

2012

Committee:
James M. Thomson
Andrew T. Jessup
Johannes R. Gemmrich

Program Authorized to Offer Degree:
UW Civil and Environmental Engineering

University of Washington

Abstract

Wave Breaking Dissipation in a Fetch-Limited Sea

Michael Schwendeman

Chair of the Supervisory Committee:
Assistant Professor James M. Thomson
UW Civil and Environmental Engineering

Coupled remote sensing and *in situ* measurements of strongly-forced, fetch-limited waves are applied to assess the role of breaking in an evolving wavefield. Wave growth follows accepted fetch-limited relations, and estimated terms in the Radiative Transfer Equation are in quasi-equilibrium. Remote sensing measurements of the Phillips breaking distribution, $\Lambda(c)$, using stabilized shipboard video recordings are unimodal and qualitatively consistent with several recent studies. *In situ* measurements of turbulent energy dissipation from wave-following "SWIFT" drifters and a tethered Dopbeam system are consistent with the wave evolution and wind input (as estimated using the Radiative Transfer Equation). The breaking strength parameter, b, is calculated by comparisons of the fifth moment of $\Lambda(c)$ with the measured dissipation rates and varies over nearly three orders of magnitude. Breaking strength is shown to negatively correlate with average wave saturation and steepness, in contrast to recent laboratory results by Drazen et al. (2008). An explanation for this difference is proposed based on the energy ratio between the peak waves and the equilibrium range.

TABLE OF CONTENTS

Page

LIST OF FIGURES

ACKNOWLEDGMENTS

PREAMBLE

The following work was performed with significant contributions from two of my committee members, Jim Thomson and Johannes Gemmrich, which should be noted in advance. The data comes from an 8-day field experiment led by them in the Strait of Juan de Fuca in February, 2011, prior to my arrival at the University of Washington. As such, I have relied heavily on their notes and memory of the experiment to guide my examination of the data. Additionally, I have utilized some of their pre-processed results, particularly *in situ* turbulence measurements of dissipation from Gemmrich's Dopbeam platform and Thomson's SWIFTs (see Chapter 2). I have also used wind results processed by Thomson from the shipboard sonic anemometer.

My contributions to the analysis have been primarily focused on the processing of video data and the synthesis of video results with turbulence and wind results. However, this video processing also relied on results published in recent years by these committee members. The practice of differencing frames to isolate breaking waves (see Chapter 2) was introduced in Gemmrich et al. (2008), and many results from that paper informed the choices outlined here. The theory of the Fourier method was previously described in Thomson and Jessup (2009). Results from experiments in Lake Washington and Puget Sound using this method were reported in Thomson et al. (2009).

The body of this thesis has been submitted as an article to the *Journal of Physical Oceanography*. For all the reasons mentioned above, these individuals will be included as co-authors on this paper. They, along with my final committee member, Andy Jessup, have been extremely valuable resources in preparing and editing this thesis. However, except where noted above, the work outlined hereafter is my own.

Chapter 1

INTRODUCTION

Surface waves are one of the most recognizable features of ocean physics. Their importance is both intellectual and practical. In particular, breaking surface waves are crucial for many aspects of air-sea interaction, such as the generation of ocean currents, transfer of gases, and turbulent mixing in the upper ocean. Waves are also a vital concern for mariners, as steep and breaking seas pose many risks to ocean vessels (Melville, 1996). Yet the history of wave research is relatively short (Young, 1999). The fundamentals of linear wave mechanics were determined by Airy, Stokes, and others in the 19th century, and the first large observational studies and resulting empirical theories of wave development were made by Sverdrup, Munk, and Bretschneider around World War II. However, modern understanding of surface waves began with the landmark studies by Phillips (1957) and Miles (1957) on the generation of wind waves and the theory of nonlinear interactions of waves developed by Hasselman (1962). From these early studies, a theoretical framework for surface wave evolution has developed.

1.1 The Radiative Transfer Equation

Surface waves are often represented by a spectrum, $E(f)$, showing the energy contained in different wave frequencies. Wave energy is proportional to the square of wave height, and this energy is moves through the wave field at the group velocity, $c_g = \partial\omega/\partial k$ (Kundu and Cohen, 2008). In deep water, there are three major processes which cause the wave spectrum to change: wind input, nonlinear interactions, and energy dissipation from wave breaking (Babanin, 2011). Thus, the evolution of the spectrum is often represented in terms of the Radiative Transfer Equation,

$$\frac{\partial E(f)}{\partial t} + c_g \cdot \nabla E(f) = S_{wind}(f) + S_{nl}(f) - S_{brk}(f) \tag{1.1}$$

where $S_{wind}(f)$, $S_{nl}(f)$, and $S_{brk}(f)$ are the source terms corresponding to wind, non-linear interactions, and breaking. Alternatively, a bulk form of the Radiative Transfer Equation can be written by integrating the terms over all frequencies,

$$\frac{\partial E}{\partial t} + c_g \cdot \nabla E = S_{wind} - S_{brk} \tag{1.2}$$

Here, the nonlinear term has been dropped as it does not change the total energy in the system, only the distribution of the energy within the spectrum. Although there is uncertainty in the form of both S_{wind} and S_{nl}, the physics of these processes is relatively well-understood, especially in comparison with the highly nonlinear process of breaking (Babanin, 2011). However, recent advancements in experimental, observational, and computational study of wave breaking show promise for the quantification of wave dissipation.

1.2 Fetch-Limited Waves

Fetch-limited conditions occur when consistent winds blow perpendicular to a coastline. After enough time has passed, the wave field becomes "steady," and only varies with the distance from the shoreline (Young, 1999). This distance is called fetch, x. Sverdrup and Munk (1947) and Kitaigorodskii (1962) examined this type of system, and determined that important variables include the variance of the water surface height, σ^2, the 10-meter wind speed, U_{10}, gravitational acceleration, g, and the peak frequency, f_p. Dimensional analysis shows that these variables can form three non-dimensional groups:

$$\hat{x} = \frac{gX}{U_{10}^2}, \quad \hat{e} = \frac{g^2\sigma^2}{U_{10}^4}, \quad \hat{f} = \frac{U_{10}f_p}{g} \tag{1.3}$$

where $\hat{x}$, $\hat{e}$, and $\hat{f}$ are non-dimensional fetch, energy, and frequency, respectively. Numerous studies (CERC, 1977; Donelan et al., 1985; Dobson et al., 1989; Donelan et al., 1992) have sought to empirically determine universal fetch relations from these groups of the form

$$\hat{e} = f_1(\hat{x}), \quad \hat{f} = f_2(\hat{x}) \tag{1.4}$$

At large fetches, many of these relations approach asymptotic limits where growth stops and the waves become "fully-developed." Several of these functions and limits have been

consolidated by Young (1999) into two equations with a range of coefficients,

$$\hat{e} = \max \begin{cases} (7.5 \pm 2.0) \times 10^{-7}\, \hat{x}^{\,0.8} \\ (3.6 \pm 0.9) \times 10^{-3} \end{cases} \tag{1.5}$$

and

$$\hat{f} = \min \begin{cases} (2.0 \pm 0.3)\hat{x}^{-0.25} \\ (0.13 \pm 0.02) \end{cases} \tag{1.6}$$

These empirical growth laws do not explicitly model the wind input or breaking dissipation terms described in the previous section, so they do not aid in physically understanding the development of fetch-limited waves. However, they do provide a baseline comparison for fetch-limited measurements like those presented in Chapter 3.

1.3 Wave Breaking

Wave breaking is the process by which steep waves become unstable and collapse, in doing so releasing some of their energy into the water column. The intermittent and highly nonlinear nature of breaking makes theoretical analysis of the process difficult (Banner et al., 2000). Even determining when a wave will break is challenging. In solving for nonlinear, finite-amplitude surface waves, Stokes showed that the maximum amplitude of such waves was $a_{max} = 0.07\lambda$, where λ is the wavelength (Kundu and Cohen, 2008). This can be rearranged in terms of wave steepness, ak, to a limiting steepness value of $ak_{max} = 0.443$. Another suggested criterion is that at breaking onset, the horizontal particle velocities at the wave crest must exceed the phase velocity (Stansell and MacFarlane, 2002). However, both these criteria and many others have so far been incomplete in determining universal breaking onset (Banner and Pierson, 2007).

Further complicating matters, identifying breaking waves can also be problematic. The most obvious signature of a breaking wave is a "whitecap," and the term "whitecapping" is often used interchangeably with the term wave breaking (Babanin, 2011). Whitecaps can be measured visually (as in Chapter 2), accoustically (Ding and Farmer, 1994), or with radar (Phillips et al., 2001). However, as first described by Banner and Phillips (1974), small "microbreaking" waves do not break with enough intensity to produce whitecaps, so these

events are often not captured with the above techniques. Jessup et al. (1997) showed that microbreaking is detectable in infrared images due to the disruption of the "cool skin" layer that exists at the water surface. Infrared measurement of breaking remains a promising, though challenging, means to measuring all breaking waves, rather than just whitecaps.

Still, some aspects of breaking have become clearer in recent years. Waves are known to break in deep water because of an instability mechanism called "modulational instability," similar to the Benjamin-Feir instability developed for nearly-linear, two-dimensional monochromatic wave trains (Babanin, 2011). The strength of this instability is related to the steepness and the spectral bandwidth of the waves in a group. It results in local energy convergence, and steepening, of the energy maximum of the wave group, which can lead to breaking (Banner and Pierson, 2007).

A fundamental attribute of breaking waves is increased steepness. Two experiments in particular make this point clear. In Banner et al. (2000), the breaking probability of dominant waves (defined as within 30% of the peak frequency) was found to correlate well with the spectral peak steepness (averaged within the same frequency range). However, this result was shown to be sensitive to the choice of spectral bandwidth around the peak, and could not easily be extended to the rest of the spectrum. Thus Banner et al. (2002) used the saturation spectrum, $B(\mathbf{k}) = k^4 \Phi(\mathbf{k})$, where $\Phi(\mathbf{k})$ is the wavenumber spectrum, to calculate spectral steepness. The saturation spectrum is a measure of wave steepness, as can be seen by its relationship with the mean-square slope:

$$\text{mss} \equiv \iint k^2 \Phi(k,\theta) \, k \, dk \, d\theta = \iint B(k,\theta) \, d(\ln k) \, d\theta \tag{1.7}$$

More specifically, Banner et al. (2002) found a correlation between breaking probability and normalized, azimuthal-integrated saturation,

$$\tilde{\sigma} = \int_0^{2\pi} \frac{B(k,\theta)}{D(k)} \, d\theta \tag{1.8}$$

where $D(k)$ is a local angular spreading width (often found empirically). $\tilde{\sigma}$ can be calculated as function of frequency from the deep-water linear dispersion relation, $f = (2\pi)^{-1}\sqrt{gk}$, as

$$\tilde{\sigma}(f) = \frac{(2\pi)^4 f^5 E(f)}{2g^2 D(f)} \tag{1.9}$$

Banner et al. (2002) noted a consistent linear correlation of breaking probability with normalized saturation, with a common threshold of $\tilde{\sigma} \sim 4.5 \times 10^{-3}$, for waves with frequencies ranging from 1 to 2.5 times the peak.

1.4 Laboratory Studies of Breaking Dissipation

The link between breaking-induced dissipation and breaking kinematics was first investigated in several laboratory experiments in the 1980s and early 1990s. Duncan (1981, 1983) studied quasi-steady breakers generated by towing a submerged hydrofoil through a long channel. These experiments indicated that the drag force, F_b, resulting from a quasi-steady breaking wave in the wake of the hydrofoil is a function of the wave phase speed, c, and the angle of the water surface in the breaking region, θ,

$$F_b = \frac{0.009 \rho_w c^4}{g \sin \theta} \tag{1.10}$$

where g is gravitational acceleration and F_b is the force per crest length. This drag force, with an additional characteristic speed, can be used to calculate the energy dissipated from the breaker. Assuming this characteristic speed is proportional to c, a scaling of the rate of energy loss to breaking per unit crest length takes the form

$$\epsilon_l \propto \frac{\rho_w c^5}{g} \tag{1.11}$$

A series of laboratory experiments in the following years (Melville and Rapp, 1985; Rapp and Melville, 1990; Lamarre and Melville, 1991; Loewen and Melville, 1991) used dispersive focusing to research unsteady breaking waves more akin to natural whitecaps than Duncan's quasi-steady breakers. Melville and Rapp (1985) provided the first measurements of momentum loss from unsteady breaking. Building from this study, Rapp and Melville (1990) is notable for its comprehensive measurements of laboratory breaking waves. Rapp and Melville (1990) used both wire wave gauges and laser Doppler velocimetry to measure the loss of momentum and energy, surface geometry, and the underwater turbulent signature caused by breaking waves. Lamarre and Melville (1991) studied the importance of bubble generation in breaking waves, and concluded that work done by the breaker to submerge the bubble plume could make up as much as 50% of the energy dissipation. Loewen and

Melville (1991) related breaking dissipation to microwave backscatter and acoustic energy. Melville (1994) used the results of Loewen and Melville (1991) to measure the dissipation rate and found that while unsteady breakers produced notably less dissipation per crest length than Duncan's quasi-steady breaking, they still nonetheless followed the scaling of Equation 1.11. However, Melville (1994) noted an additional trend of increasing ϵ_l with larger wave slopes.

While these later laboratory experiments better simulate the unsteady nature of true ocean whitecaps, they still lack some of the physics. Most importantly, they are driven to break by steepening caused by the linear superposition of waves, rather than the nonlinear modulational instability of wave groups. In addition, they lack the directionality and short-crestedness of ocean waves (Babanin, 2011).

1.5   Dissipation in the Equilibrium Range

The results of Phillips (1985) are integral to the work described throughout this thesis. In this study, Phillips revisited his own earlier (Phillips, 1958) prediction of an upper-limit spectral asymptote of the form

$$E(f) \propto g^2 f^{-5} \tag{1.12}$$

This limit was based on the premise of constant saturation (note the similarity to Equation 1.9), such that any excursions of spectral density would immediately be dissipated by breaking. The high frequencies where this spectrum appeared to apply he called the "equilibrium range." However, Toba (1973) showed that his wind-tunnel data actually better followed the form

$$E(f) \propto u_* g f^{-4} \tag{1.13}$$

where u_* is the wind friction velocity. This new form was supported by the field observations of Kawai et al. (1977), Donelan et al. (1985), among others. Kitaigorodskii (1983) used a Kolmogorov-type argument to support Toba's relation. In his hypothesis, wind input, spectral flux divergence, and dissipation are all negligible in the equilibrium range, and energy cascades from its input at large, energy-containing waves to dissipation at very high

frequencies. Phillips (1985) used a different argument to obtain Toba's spectral form. In Phillips's analysis, he assumed a balance between the input, dissipation, and nonlinear source terms, where the terms are all important (i.e. non-trivial) and in local equilibrium. Thus he argued that the terms must be proportional, and with estimates of the wind input function and nonlinear flux divergence, predicted the form of the dissipation function as

$$\epsilon(k, \theta) \, dk \, d\theta = 2\gamma\beta^3(\cos\theta)^{3p}u_*^3 k^{-1} \, dk \, d\theta \tag{1.14}$$

Or, with the dispersion relation,

$$\epsilon(c, \theta) \, dc \, d\theta = 4\gamma\beta^3(\cos\theta)^{3p}u_*^3 c^{-1} \, dc \, d\theta \tag{1.15}$$

where γ, β, and p are empirical coefficients.

Phillips (1985) used this result to make a prediction of the wave breaking that would be needed to fit this dissipation function. He introduced a statistical description of breaking, $\Lambda(c, \theta)$, which is defined as the distribution of breaking crest length per area as a function of speed, c, and direction, θ. Thus the total length of breaking crests per area is

$$L_{total} = \int_0^\infty \int_0^{2\pi} \Lambda(c, \theta) d\theta dc \tag{1.16}$$

The omnidirectional distribution, $\Lambda(c)$, is often used in place of the full directional distribution. It can be found by integrating over all directions in broad-banded waves or by using the speed in the dominant direction in sufficiently narrow-banded wavefields. The breaking rate, or breaker passage rate, is the frequency that an actively breaking crest will pass a fixed point in space. One obtains the breaking rate from the first moment of $\Lambda(c)$,

$$R = \int c\Lambda(c)dc \tag{1.17}$$

Wave dynamics can be related to the $\Lambda(c)$ distribution based on the scaling of energy dissipation per crest length of Equation 1.11. Since $\Lambda(c)$ gives the total normalized breaking crest length at speed c, $\Lambda(c)$ is related to the energy dissipation due to wave-breaking, $\epsilon(c)$, through

$$\epsilon(c) \, dc = \frac{b\rho_w}{g} c^5 \Lambda(c) \, dc \tag{1.18}$$

where b is a "breaking strength" proportionality factor. From Equations 1.15 and 1.18, Phillips (1985) predicted $\Lambda(c)$ to be of the form

$$\Lambda(c) = (4\gamma\beta^3)I(3p)b^{-1}u_*^3 gc^{-6}, \tag{1.19}$$

where

$$I(3p) = \int_{-\pi/2}^{\pi/2}(\cos\theta)^{3p}d\theta \tag{1.20}$$

1.6 Observations of $\Lambda(c)$

Phillips et al. (2001) produced the first field observations of $\Lambda(c)$, using backscatter and power from radar data. They found energy dissipation, from $c^5\Lambda(c)$, to be broadly distributed among speeds above about 3 m s^{-1}. They hypothesized that the drop-off at low speeds, corresponding to a unimodal $\Lambda(c)$ distribution, was due to missing small, weak events that did not produce foam. They also showed no evidence of a "Kolmogorov cascade" in wave breaking, asserted by Kitaigorodskii (1983) and others. Melville and Matusov (2002) used digital video taken from an airplane to calculate $\Lambda(c)$. They presented a monotonically decreasing distribution of the form $\Lambda(c) = (3.3 \times 10^{-4})(U_{10}/10)^3 e^{-0.64c}$ (with SI units). However, they had limited resolution and used the assumption that the rear of breaking crests was stationary.

In recent years, there has been emerging consensus that $\Lambda(c)$ actually shows a peaked distribution, at least for whitecaps. Plant (2012) suggested as a mechanism for this peaked distribution the large slopes produced by an interference pattern of dominant wind waves, moving at speeds slightly less than the group velocity. By simulating this interference pattern from a representative wave spectrum, he showed that he could accurately predict the peak speed of breaking, as measured by a number of methods, including $\Lambda(c)$. Gemmrich et al. (2008) calculated a peaked distribution using video taken from the Research Platform *FLIP*. They fit an ellipse to the forward edge of each breaking crest, and used the major axis for the crest length and translation of the centroid for breaking speed. This study is notable for the high spatial resolution of their video (pixel size of $1.9-3.2\times 10^{-2}$ m), which resolved even the smallest scales of whitecaps. In addition, they observed a correlation between the

breaking rate and the mean normalized saturation, σ_b. Kleiss and Melville (2010) calculated $\Lambda(c)$ distributions in strongly-forced, fetch-limited seas during the Gulf of Tehuantepec Experiment (GOTEX). They used a temporally and spatially varying definition of the breaking crest speed, which they called the "elemental method." They estimate the coefficients in Equation 1.19, and explicitly show that their unimodal distributions do not follow Phillips's predicted form. Rather, their $\Lambda(c)$ are shown to closely follow a Rayleigh distribution, though no physical reason for this is apparent. Kleiss and Melville (2011) further detailed this method and demonstrated that the differing results from Melville and Matusov (2002) and Gemmrich et al. (2008) could be reproduced in their data by imitating each study's video processing method.

Thomson and Jessup (2009) introduced a Fourier-based method for processing video data into $\Lambda(c)$ distributions, which was applied in Thomson et al. (2009) for data taken in Lake Washington and Puget Sound. The Fourier-based method has the advantage of increased efficiency and robust statistics compared to conventional time-domain crest-tracking methods. They used the subtraction of subsequent frames, as in Gemmrich et al. (2008), to isolate breaking crests. They used the method of Chickadel et al. (2003) to transform the resulting frequency-wavenumber spectrum to a speed spectrum. In Thomson and Jessup (2009), the Fourier method was validated alongside an algorithm similar to the one used in Gemmrich et al. (2008). This Fourier method is used, with some modifications, in this thesis. It is described in more detail in Chapter 2.

Two additional observations of breaking distributions should be noted. Although they did not calculate $\Lambda(c)$, Ding and Farmer (1994) used passive acoustics with an array of hydrophones to track and measure the phase speed of breaking waves. They calculated a breaking probability density function that closely resembles later observed $\Lambda(c)$ curves. The breaking probability is broadband in speed, and centered around half the dominant phase speed. Finally, Jessup and Phadnis (2005) were the first to include microbreaking in calculating $\Lambda(c)$. They used a particle image velocimetry (PIV) algorithm on infrared imagery of wave breaking in a laboratory wind-wave tank. Again, for a range of wind speeds and tracking methods, the $\Lambda(c)$ distributions are centered roughly around half the peak phase speed.

1.7   Total Dissipation from $\Lambda(c)$

Phillips (1985) derived the relation of Equation 1.19 from his analysis of the spectral source terms in the equilibrium range, so it is only expected to be valid within this range. The total (non-spectral) energy dissipation from breaking, however, can be calculated from $\Lambda(c)$ independent of this theoretical prediction. From 1.18 the total rate of energy lost is

$$\dot{E} = \int \epsilon(c)\,dc = \frac{b\rho_w}{g} \int c^5 \Lambda(c)\,dc \tag{1.21}$$

Equation 1.21 has shown promise for remote sensing quantification of energy dissipation. The key to the remote calculation of dissipation is knowledge of the form of b. Estimates of b have varied widely in the literature, however. They have been made in studies of quasi-steady breaking, laboratory breaking using dispersive focusing techniques, and remote field studies. Drazen et al. (2008) provide a summary of b measurements prior to 2008. Values of b have spanned four orders of magnitude, from 3.2×10^{-5} in Gemmrich et al. (2008) to 7.5×10^{-2} in Duncan (1983). Confounding the issue is uncertainty over the nature of b. In introducing the concept, Phillips (1985) treated b as a constant, but a number of laboratory experiments have noted dependencies of b on the wave slope (Duncan, 1981; Melville, 1994) or growth rate (Banner and Pierson, 2007).

Drazen et al. (2008) used an inertial model of a plunging breaking wave to produce a scaling of b of the form,

$$b \propto (hk)^{5/2} \tag{1.22}$$

Laboratory data from breakers generated using linear superposition support this scaling. Based on these results, Romero et al. (2012) proposed two spectral models of b for breaking in the Gulf of Tehuantepec Experiment (GOTEX),

$$b_1(k) = A_1(B(k)^{1/2} - B_T(k)^{1/2})^{5/2} \tag{1.23}$$

and

$$b_2(k) = A_2(\tilde{B}(k)^{1/2} - \tilde{B}_T(k)^{1/2})^{5/2} \tag{1.24}$$

where $B(k)$ is the spectral saturation in wavenumber, $\tilde{B}(k)$ is the normalized saturation, and A_1, A_2, $B_T(k)$, and $\tilde{B}_T(k)$ are coefficients fit to their data. These models are related to the prediction of Equation 1.22 using the fact that $B(k)$ is related to the mean-square-slope (mss) through Equation 1.7. Calculation of $b(k)$ by Romero et al. (2012) showed moderate agreement with this model, but this agreement is sensitive to their wind input function and the measurement of the saturation spectrum. They improved their model by normalizing their $B(k)$, $\tilde{B}(k)$, and $b(k)$ by the wavenumber at the peak of these functions. They were unable to reconcile the lack of visible breaking at low speeds, yielding unreasonably high b values for high wavenumbers.

In this thesis, the assumption of a "bulk" breaking strength, where b is not a function of c, is used. Although b is assumed constant for all speeds of breaking, it may vary with other characteristics of the wave field, such as wave age, steepness, or mean saturation. This is similar to the analysis used in Gemmrich et al. (2008). They showed a correlation of increasing b with wave age, $c_p u_*^{-1}$. This bulk breaking strength assumption is discussed more in Chapter 5.

1.8 Other Measures of Dissipation

Calculation of b requires a separate measurement of the breaking dissipation. However, direct *in situ* measurements of dissipation in the water column during breaking have been rare and are difficult to make (Terray et al., 1996; Gemmrich and Farmer, 2004). In the absence of *in situ* measurements, Gemmrich et al. (2008) and Romero et al. (2012) used indirect estimates of dissipation from wind measurements and wave spectra. Gemmrich et al. (2008) used the parameterization of Gemmrich et al. (1994),

$$S_{wind} = \rho_a c_{eff} u_*^2 \tag{1.25}$$

where c_{eff} is the effective phase speed of the waves acquiring energy from the wind. Terray et al. (1996) calculated c_{eff} from *in situ* turbulence measurements from a number of field experiments under a variety of conditions. In nearly fully-developed waves, they found c_{eff} normalized by peak phase speed to be weakly related to wave age, $u_* c_p^{-1}$. For $u_* c_p^{-1} \geq 0.08$, however, $c_{eff} c_p^{-1}$ values grouped around roughly 0.5 and showed much scatter. For their

wind input, Romero et al. (2012) use three spectral input functions: from Snyder et al. (1981), Janssen (1991), and a modified form of Janssen (1991) including the effects of long waves "sheltering" smaller short waves. These three models are all derived from the wind input theory of Miles (1957), which attributes wave growth to pressure perturbations from a quasi-laminar shear flow (Young, 1999).

Alternatively, *in situ* turbulence dissipation measurements can be used as a proxy for breaking dissipation. Dissipation in a turbulent boundary layer over a flat, rigid, wall obeys a "law of the wall" scaling,

$$\epsilon = \frac{u_*^3}{\kappa z} \tag{1.26}$$

where z is the distance from the interface and κ is the von Kármán constant. Numerous studies (Kitaigorodskii et al., 1983; Agrawal et al., 1992; Anis and Moum, 1995) have shown a layer of enhanced dissipation under breaking waves, decaying significantly faster than the law of the wall solution. Below this enhanced layer, measurements tend to approach the expected law of the wall scaling. Gemmrich and Farmer (2004) correlated enhanced dissipation with breaking events, indicating that dissipation in this surface layer corresponds to energy lost from waves.

Gemmrich (2010) measured turbulent dissipation using a system of three high-resolution pulse-coherent Sontek Dopbeam acoustic Doppler profilers. He was able to measure dissipation even into the wave crest, above the mean water line. He found that turbulence was enhanced particularly in the crest, even more so than previous observations. Thomson (2012) achieved a similar result with wave-following "SWIFT" drifters, which measure turbulent dissipation from near the surface to a half meter below the surface with a pulse-coherent Aquadopp acoustic Doppler profiler. Both these studies measured dissipation using the second-order structure function, $D(z, r)$, as described in detail in Section 2.

1.9 Thesis Outline

This thesis describes field observations of wave breaking made under fetch-limited conditions in the Strait of Juan de Fuca, WA. In Chapter 2, the field experiment is described and the methods are summarized. The direct results of the video observations and *in situ*

measurements are reported in Chapter 3. Chapter 4 presents the combined results: the analysis of the energy budget and estimates of b. In Chapter 5, these results are compared with the predictions of Phillips (1985) and Drazen et al. (2008), as well as other field studies.

Chapter 2

METHODS

2.1 Collection of Field Data

Observations were made in the Strait of Juan de Fuca (48°12' N 122°55' W), north of Sequim, Washington, from February 12-19, 2011. Measurements were taken onboard the R/V *Robertson* and from two free-floating "SWIFT" (Surface Wave Instrument Float with Tracking) drifters. The roughest conditions were observed during the days of February 14th and 15th, in which a winter storm hit the region with consistent southerly winds of 9-18 ms^{-1}. On these days, the *Robertson* was set on a drogue and allowed to drift across the Strait (downwind) at approximately 2 km hr^{-1}. Wave height and period increased along track, as shown in Figure 2.1.

Wave breaking observations were made from a video camera mounted above the *Robertson* wheelhouse, at 7 m above the mean water level, aimed off the port side of the ship. With the drogue set from the stern, the port side view was an undisturbed wavefield. The video camera was equipped with a 1/3" Hi-Res Sony ExView B&W CCD. The data (eight-bit grayscale, 640 × 480 pixel, NTSC) was sampled at 30 Hz and later subsampled to 15 Hz. The lens had a 92° horizontal field of view and was oriented downward at an incidence angle of approximately 70 degrees, giving a pixel resolution of 10-40 cm in the analyzed region. The video was stabilized in the vertical and azimuthal (pitch and yaw) directions with a pan-tilt mounting system (Directed Perception PTU-D100). The camera position was remotely reset periodically, as it was prone to drift in the azimuth at frequencies on the order of 5° per minute. Short video windows of 5 to 10 minutes were chosen for analysis to avoid these resets and ensure statistical stationarity of the breaking conditions.

Wave and turbulence measurements were made from the two wave-following SWIFT drifters. These Lagrangian drifters are described in detail in Thomson (2012). They were equipped with a QStarz BT-Q1000eX, 5 Hz GPS logger and accelerometer, 2 MHz Nortek
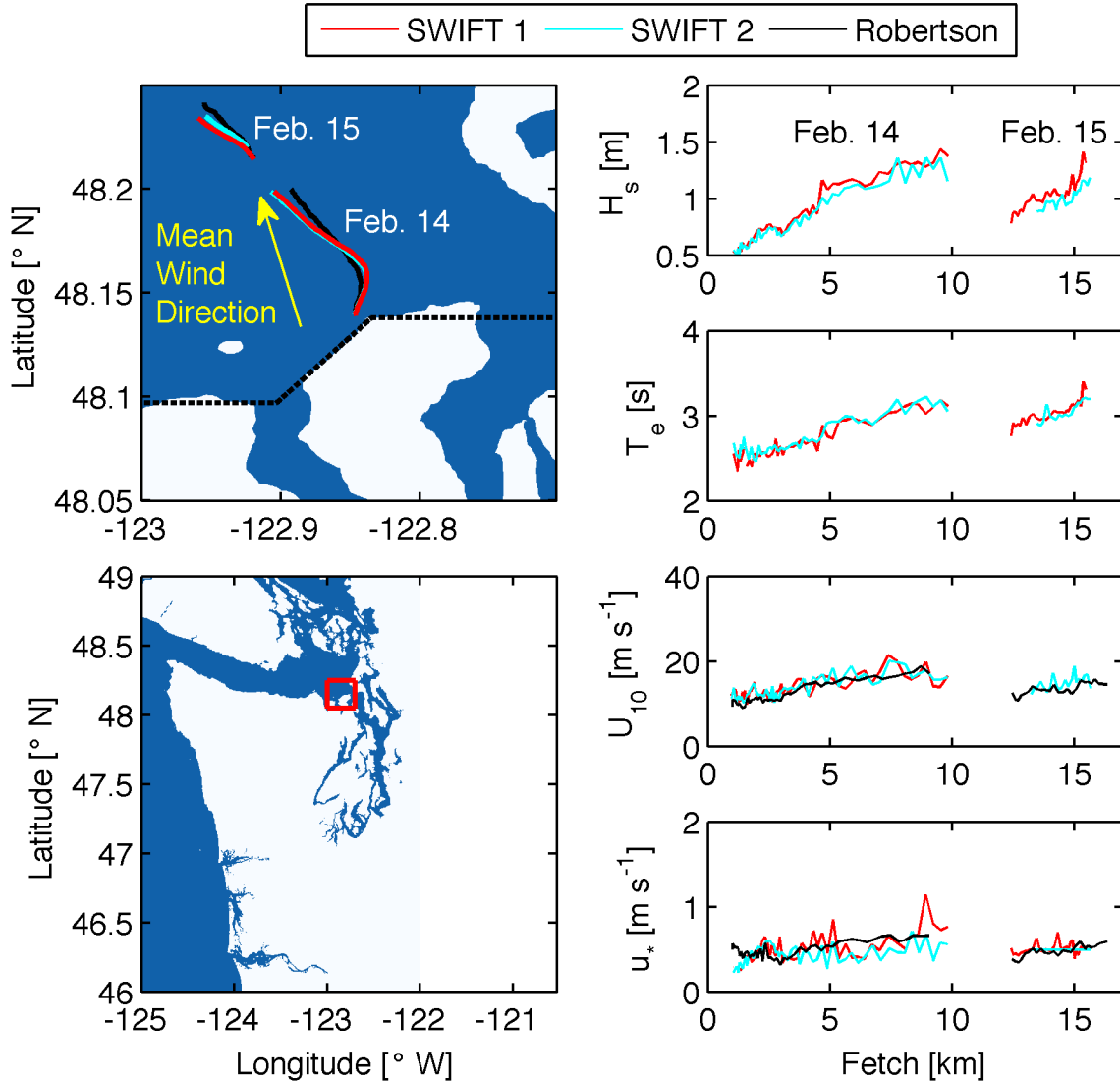
Figure 2.1: Summary of conditions during the two days of observations. Bottom left: a map of Pacific Northwest showing the Strait of Juan de Fuca. The red box corresponds to the edges of the top left map. Top left: map of instrument and ship tracks during February 14 and 15. The dashed line is the zero-fetch line. The solid lines are the tracks of the *R/V Robertson* and Dopbeam (black), SWIFT 1 (red), and SWIFT 2 (cyan). The yellow arrow shows the average direction of the wind from both days. The right panels show the evolution of the wave and wind conditions with fetch measured from SWIFT 1 (red), SWIFT 2 (cyan), and the *R/V Robertson*(black in wind measurements). Conditions shown are significant wave height (top), peak energy period (upper middle), 10-meter wind speed (lower middle), and friction velocity (bottom).

Aquadopp HR pulse-coherent Acoustic Doppler Current Profiler (ADCP) with 4 Hz and 4 cm bin size, Go-Pro Hero digital video camera, and Kestral 4500 anemometer. The SWIFTs were released from the *Robertson* and generally drifted at similar speeds, thus staying within approximately 1 km of the ship. Similar turbulence measurements were made from Sontek Dopbeam pulse-coherent acoustic Doppler profilers tethered to the ship on a wave-following platform. This Dopbeam system is discussed further in Gemmrich (2010).

Wave spectra and associated parameters were estimated using the orbital velocities measured by Doppler speed-resolving GPS loggers onboard the freely-drifting SWIFTs, using the method of Herbers et al. (2012). Wind measurements were made from the SWIFTs at 0.9 m above the water surface, as well as from the shipboard sonic anemometer (RM Young 8100), at a height of 8.9 m. The wind friction velocity u_* was estimated using the inertial dissipation method as described in Yelland et al. (1994).

2.2   *Video Processing for the Distribution of Breaking Crests,* $\Lambda(c)$

The method of Thomson and Jessup (2009) is used to process the video recordings of wave-breaking and determine the crest-length distributions $\Lambda(c)$. A short summary is provided below, along with four notable modifications. For reference on the sensitivity of $\Lambda(c)$ to different methods of processing, see Kleiss and Melville (2011).

The analysis begins with the rectification of camera pixels to real-world coordinates using the methods of Holland et al. (1997). Here the x and y directions are taken as the along-ship and cross-ship directions, respectively. A portion of the image, roughly 15 m $\times$ 20 m and no closer than 15 m from the ship is extracted and interpolated to a uniform grid of 2^n points. This field of view is notably less than in Kleiss and Melville (2010) (roughly 0.2 km^2), however it is sufficient to capture complete crests for the conditions observed. The resulting pixel resolution is around 0.25 m (cross wave) by 0.075 m (along wave).

Video is broken up into segments of 1024 frames (68.3 seconds) with 25% overlap. Sequential images are subtracted to create difference images, which highlight the moving features of the video, most prominently the leading edge of breaking waves. The breaking crests are further isolated when the differenced images are thresholded to binary images, $I(x, y, t)$ (see below for choice of threshold). This procedure was originally described in

Gemmrich et al. (2008). An example of the progression from raw image to binary is shown in Figure 2.2.

A three-dimensional fast Fourier Transform (FFT) is performed on the binary video data, which is then filtered in wavenumber to isolate the crest motion. Integration over the k_y component produces a two-dimensional frequency-wavenumber spectrum, $S(k_x, f)$, as shown in Figure 2a of Thomson and Jessup (2009). Following the method of Chickadel et al. (2003), the frequency-wavenumber spectrum is transformed to a speed-wavenumber spectrum using $c = f/k_x$, and the Jacobian $|\partial f/\partial c| = |k_x|$ preserves the variance in the spectrum. The speed spectrum is calculated by integrating over the wavenumber, $S(c) = \int S(k_x, c)dk_x$. This speed spectrum has the shape of the $\Lambda(c)$ distribution, but it must be normalized to have the correct magnitude. The normalization follows from a direct calculation of the average breaking length per unit area, L_{total},

$$L_{total} = dy\frac{\sum I(x, y, t)}{NA},$$ (2.1)

where dy is the length of the pixels along the crests, $\sum I(x, y, t)$ is the number of breaking pixels, N is the number of frames, and A is the area of our field of view. Thus, $\Lambda(c)$ is calculated as

$$\Lambda(c) = L_{total}\frac{S(c)}{\int S(c)dc},$$ (2.2)

directly following Thomson and Jessup (2009). Modifications to Thomson and Jessup (2009) are described below.

2.2.1   Calculation of Incidence Angle from Horizon

The camera incidence angle was not constant, because of the slow drift and periodic resetting of the stabilized pan and tilt. The stabilized pan and tilt adequately removed wave motions (e.g. ship roll at periods of a few seconds) from the video recordings, but contamination from lower period motions is evident in the raw video data. To remove these motions, the horizon in the undistorted image (i.e. after lens "barrel" distortion is removed) is used as a constant reference. First, the angle above horizontal is calculated as

$$\beta = \frac{y_{top} - y_{horizon}}{y_{top} - y_{bottom}} \times 69°$$ (2.3)
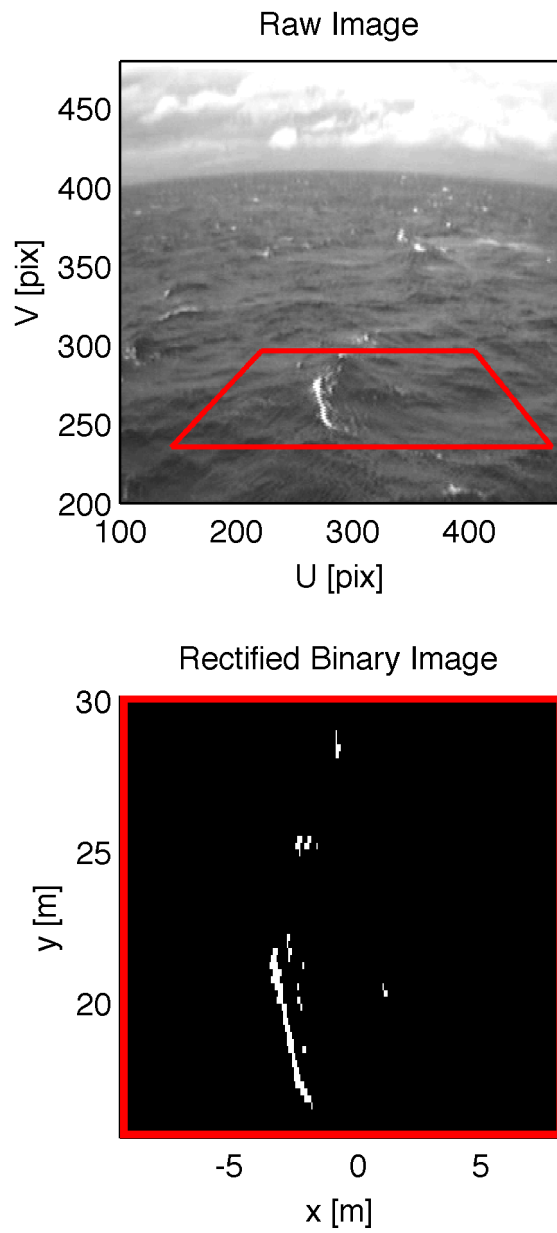
Figure 2.2: Top: video frame in raw pixel coordinates, the red box is the sampled field of view. Bottom: binary-thresholded differenced image from same frame as upper left, rectified to real-world coordinates.

where 69° is the total vertical field of view and y is in pixels. Then, the incidence angle is calculated simply as

$$\theta = 90 - 69°/2 + \beta \qquad (2.4)$$

In practice, the horizon is manually identified in four images every 30 seconds and the average value of the resulting incidence angle is used for all images in that 30 seconds. The incidence angle is essential for rectifying the video data to real-world coordinates (Holland et al., 1997).

2.2.2 Difference Threshold

Choosing an accurate binary threshold to identify breaking crests is critical to obtaining the correct $\Lambda(c)$ distribution. Differences in lighting and foam conditions make it difficult to determine a single threshold criterion. In Thomson and Jessup (2009), a threshold based on a multiple of the image standard deviation is used, with similar results over a range of conditions. In the present study, however, the wider range of conditions necessitate a more adaptable method. We use a modification of a technique described in Kleiss and Melville (2011) based on the cumulative complementary distribution of pixels

$$W(i_t) = 1 - \int_{-\infty}^{i_t} p(i)di, \qquad (2.5)$$

where $p(i)$ is the probability density function of the subtracted brightnesses. The main difference from Kleiss and Melville (2011) is the use of the differenced images rather than the raw frames. As shown in Kleiss and Melville (2011) Figure 3, $W(i_t)$ decreases from 1 to 0 as i_t increases, and shows a distinct tail at high i_t when breaking is present. This signature is also present when using differenced images. The tail is seen clearly in the second derivative of the log of $W(i_t)$, L''. As noted by Kleiss and Melville (2011), taking the threshold as the beginning of this deviation (i.e. maximum L'') produces a number of false positives in their data. To obtain better signal-to-noise, they settle on a threshold value where L'' falls to 20% of its maximum value. Here, we apply the same threshold, after manually confirming that this is near the point when thresholding stops excluding more residual foam and begins cutting off the edges of true breaking crests.

2.2.3 Constant Signal-to-Noise Filter

Thomson and Jessup (2009) describe the need to isolate the significant bands around the peak in the wavenumber-frequency spectrum when transforming to $S(c)$ to prevent noise from biasing the speed signal (page 1667). To this end, Thomson and Jessup (2009) restrict the integration from $S(k_y, f)$ to $S(k_y, c)$ to the points where the value of $S(k_y, f)$ is greater than 50% of the peak of $S(k_y)$. This process was slightly modified after examining the accuracy of the Fourier method with synthetic data. It was found that significant gains in accuracy could be made by using an integration cut-off that did not vary with wavenumber, as shown in Figure 2.3. The true $\Lambda(c)$ curve in Figure 2.3 is calculated directly from the synthetic data. For more discussion of the synthetic data and its utility in investigating the response of the Fourier method, see Appendix A. The "original" $\Lambda(c)$ distribution comes from the Fourier method as described in Thomson and Jessup (2009). For the "modified" curve, values from wavenumbers or frequencies less than 0.2 s^{-1} or m^{-1} are removed as they contain a high density of noise. Next, a constant cut-off 5% of the absolute maximum value of the remaining spectrum is used in the limits of integration around the significant band. It was found that this procedure reduced the error in the Fourier method from an average of 52% to 22% across all speeds, when weighted by the true value of $\Lambda(c)$.

2.2.4 Width/Speed Bias

A central assumption in the normalization of $\Lambda(c)$ by L_{total} described above is that the width of the breaking crests is exactly one pixel, so that all $\sum I(x, y, t)$ pixels contribute to the length of the crest. However, breaking that occurs at speeds faster than one pixel per frame, $c > \Delta x / \Delta t$, will produce crests in the binary image of width

$$n = \frac{c}{\Delta x / \Delta t},$$
(2.6)

where Δx is the pixel width in the breaking direction and Δt is the separation between frames (here, 0.0667 seconds). Evidence of this effect is shown in Figure 2.4 (top), where the average horizontal advancement of crests is plotted against their average width, weighted by crest size. These variables are well-correlated, and the relation follows closely the one-to-one line predicted by Equation 2.6. To correct for the associated bias of additional pixels

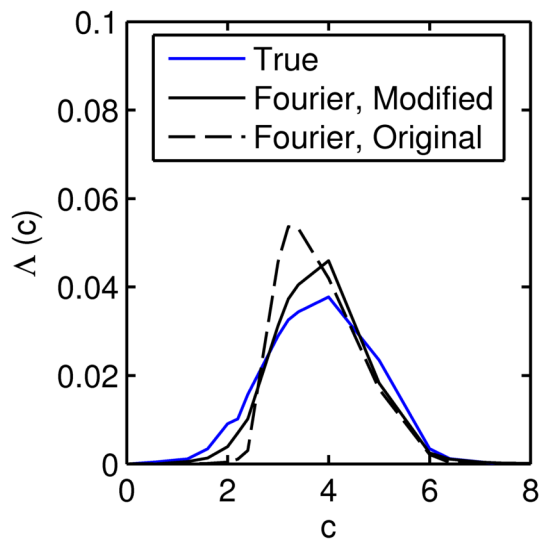Figure 2.3: Comparison of $\Lambda(c)$ results from the Fourier method with synthetic data input. The "true" distribution (solid blue) is measured directly from the synthetic data. The "original" Fourier method curve (dashed black) uses the wavenumber-specific signal-to-noise filtering of Thomson and Jessup (2009). The "modified" Fourier method (solid black) uses a constant signal-to-noise cut-off throughout the spectrum.

with fasters crests, we modify the FFT normalization of Thomson & Jessup (2009) with the ratio of $\Delta x/\Delta t$ and obtain

$$\Lambda(c) = L_{total} \frac{\Delta x/\Delta t}{c} \frac{S(c)}{\int S(c)dc}. \tag{2.7}$$

With Equation 2.1, this is equivalent to matching the first moment of $\Lambda(c)$ with the breaking rate, calculated directly from the binary images as

$$f_{brk} = \frac{\sum I(x,y,t)}{n_x n_y N \Delta t}, \tag{2.8}$$

where n_x and n_y are the number of pixels in x and y. Carrying through the integration in Equation 1.17 with the modified $\Lambda(c)$ from Equation 2.7 results in an equivalent expression as Equation 2.8. Figure 2.4 (bottom) shows both the breaking rate from the original $\Lambda(c)$ distribution, as well as from the width corrected $\Lambda(c)$, versus the direct breaking rate, f_{brk}. The linear trend in the original results indicates that the bias is small and linear. The final results are constrained to always equal the direct breaking rate.

2.3 In Situ Estimates of Energy Dissipation, $\dot{E}$

The rate of energy dissipation via wave breaking, $\dot{E}$, is estimated using *in situ* measurements of turbulent velocity profiles $u(z)$ in a reference frame moving with the wave surface. This is done from two SWIFT drifters, as described in Thomson (2012) and, independently, from a tethered Dopbeam system, as described in Gemmrich (2010). The volumetric dissipation rate $\epsilon(z)$ is calculated by fitting a power law to the observed turbulent structure function,

$$D(z,r) = \langle (u'(z) - u'(z+r))^2 \rangle = A(z)r^{2/3} + N \tag{2.9}$$

where z is measured in the wave-following reference frame (i.e. $z = 0$ is the water surface), r is the lag distance between measurements (corresponding to eddy scale), A is the fitted parameter, and N is a noise offset. Then, the depth-integrated dissipation rate is calculated as

$$\dot{E}_{SWIFT} = \rho_w \int_{0.6}^{0} \epsilon(z)dz = \rho_w \mathcal{C}_v^3 \int_{0.6}^{0} Az^{-3/2}dz, \tag{2.10}$$

where C_v is a constant equal to 1.45. The structure function is averaged over 5 minute intervals before calculating the dissipation. In addition, profiles of $\epsilon(z)$ are removed if the
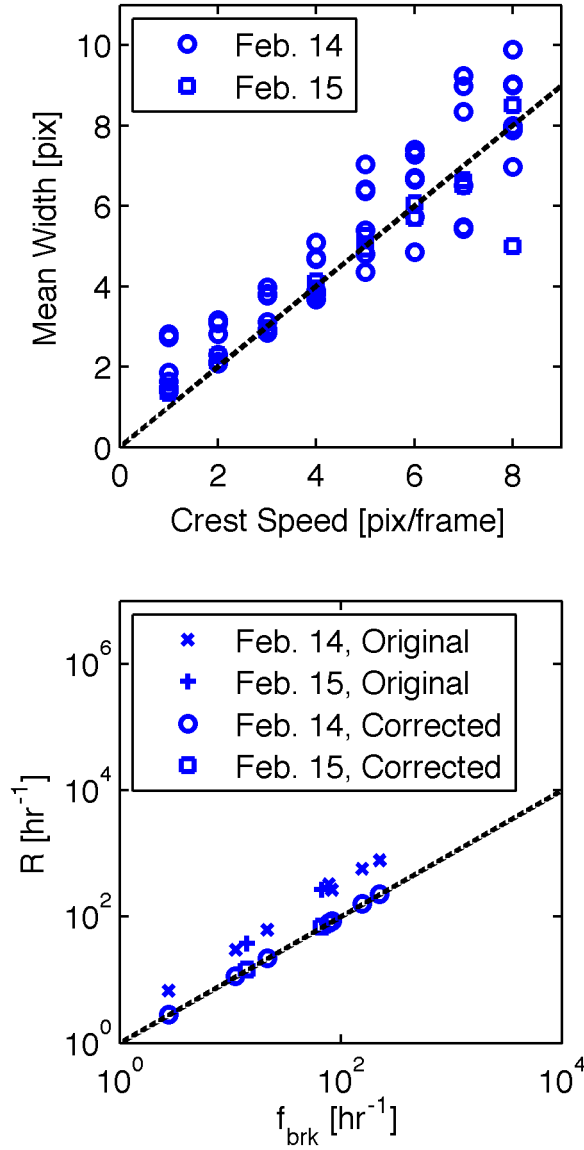
Figure 2.4: Top: comparison of mean crest width in pixels with crest advancement speed in pixels for both February 14 (circles) and February 15 (squares). Bottom: comparison of calculated breaking rate from the first moment of $\Lambda(c)$, R, with the direct breaking rate f_{brk} for the original distribution. R are shown without width correction ("original," x's for February 14, crosses for February 15), and with width correction ("corrected," circles for February 14, squares for February 15).
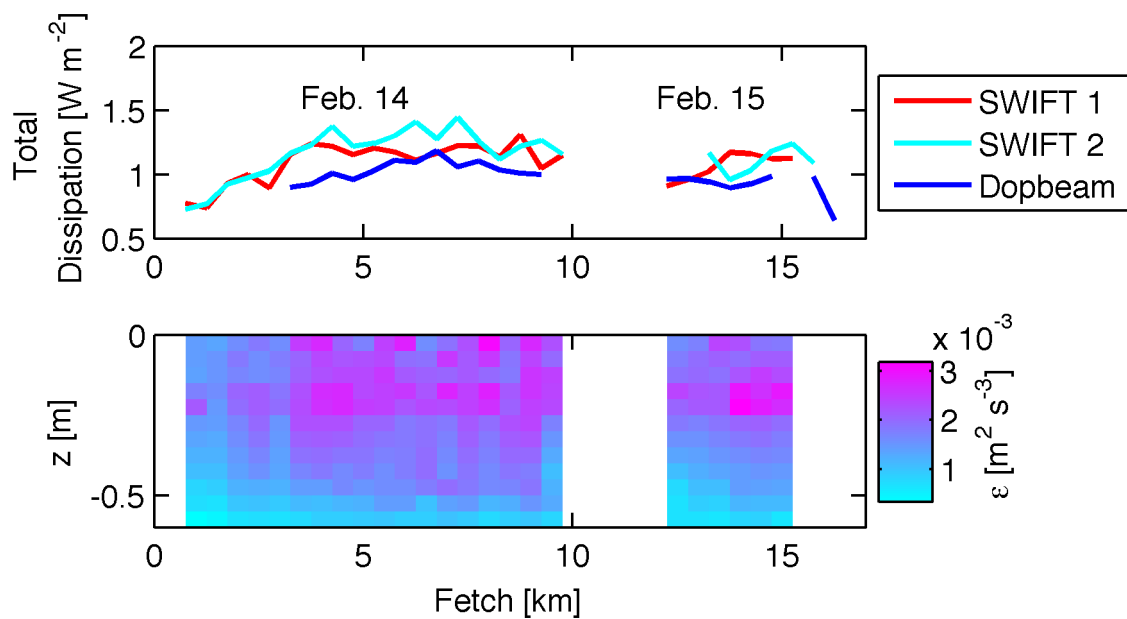
Figure 2.5: Top: total (integrated) turbulent dissipation measured by SWIFT 1 (red), SWIFT 2 (cyan), and Dopbeam (blue) vs. fetch, averaged over 500 meters. Bottom: turbulent dissipation profiles in the wave reference frame from SWIFT 1 and plotted with fetch.

$r^{2/3}$ fit does not account for at least 80% of the variance or if A is similar to N. Figure 2.5 shows the evolution of the dissipation profiles and total dissipation with fetch. Profiles of dissipation deepen, and the overall magnitude increases, as waves grow along fetch and breaking increases.

Chapter 3

RESULTS

3.1 Fetch Dependence

A number of studies have attempted to describe the evolution of a wave field under fetch-limited conditions through empirical fits to observed data (CERC, 1977; Donelan et al., 1985; Dobson et al., 1989; Donelan et al., 1992). These empirical fits use non-dimensionalized measures of fetch, wave energy, and frequency, specifically,

$$\hat{x} = \frac{gX}{U_{10}^2}, \quad \hat{e} = \frac{g^2\sigma^2}{U_{10}^4}, \quad \hat{f} = \frac{U_{10}f_p}{g} \tag{3.1}$$

where X is fetch, U_{10} is wind speed at 10 m reference height, g is gravity, σ^2 is the variance of the frequency spectrum (equivalent to the energy or $H_s^2/16$), and f_p is the frequency at the peak of the wave spectrum. Young (1999) consolidated many of these relations into two power laws with a small range of coefficients. Figure 3.1 compares this current data set against Young's empirical prediction, using 500-meter along-fetch averaging. The maximum daily 500-meter average wind speed is used for U_{10}. The $\hat{e}$ and $\hat{f}$ values lie largely above, but in line with, Young's empirical formulae. This suggests a slight underestimate of fetch, possibly due to wave generation south of the study area in Discovery Bay or Admiralty Inlet. Additionally, some scatter may be caused by variations in the wind speed throughout the day. In particular, the wave energy growth on February 15th appears steeper than given by the empirical growth law, perhaps due to a ramping up of the wind over the course of that day. In general, the observed wave height and frequency have the trends and approximate magnitude expected from fetch-limited growth, and lie well beneath fully-developed conditions.

3.2 Evolution of the Frequency Spectrum, $E(f)$

In addition to the trends in bulk parameters along the fetch, the wave frequency spectrum, $E(f)$, also evolves along the fetch. Figure 3.2 (top) shows the 500-meter averaged non-
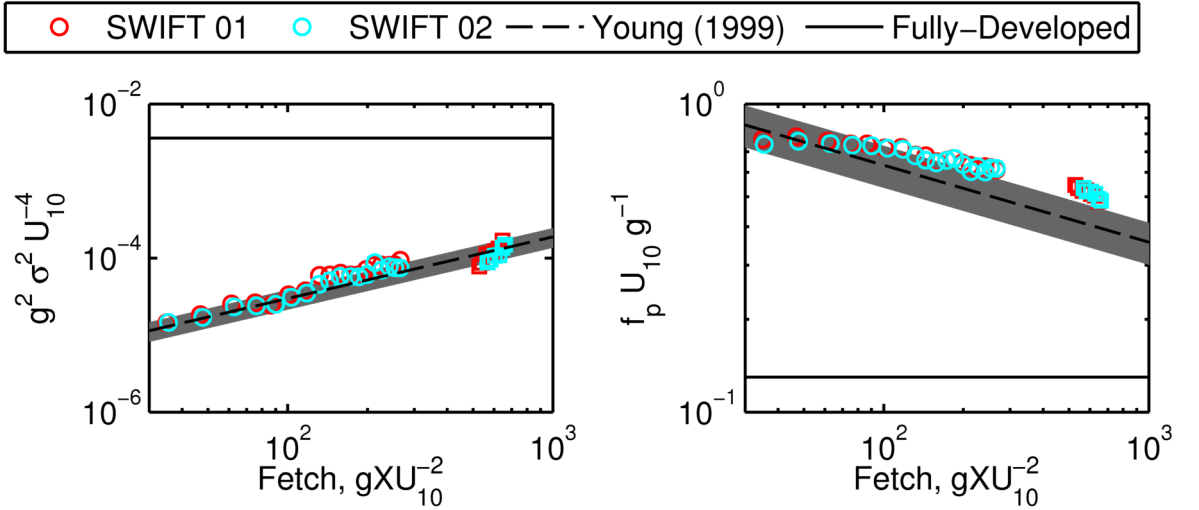
Figure 3.1: Comparison of measured wave evolution from SWIFT 1 (red) and SWIFT 2 (cyan) with the Young (1999) empirical formula (black dashed line) and fully-developed limits (horizontal solid black line). Left: dimensionless wave energy vs. dimensionless fetch. Right: dimensionless frequency vs. dimensionless fetch. The circles and squares denote data from February 14th and February 15th, respectively. All U_{10} are maximum daily 500-m averages.

dimensional energy spectra from February 14th and 15th colored by non-dimensional fetch. The spectra are normalized by maximum daily 500-meter average U_{10} similar to Figure 3.1. As shown with the bulk parameters, the peak waves grow and lengthen (shift to lower frequencies) with increasing fetch. All spectra have a high-frequency tail with an expected f^{-4} slope characteristic of the equilibrium range. It is in this range that Phillips developed the theoretical form for the $\Lambda(c)$ distribution, Equation 1.19. It is interesting to note that while there is a clear trend in the development of the peak with fetch, the energy in the equilibrium range stays relatively steady throughout the experiment (relative to the wind speed).

This is further investigated using the normalized saturation spectrum,

$$\tilde{B}(f) = \frac{(2\pi)^4 f^5 E(f)}{2g^2 D(f)} \tag{3.2}$$

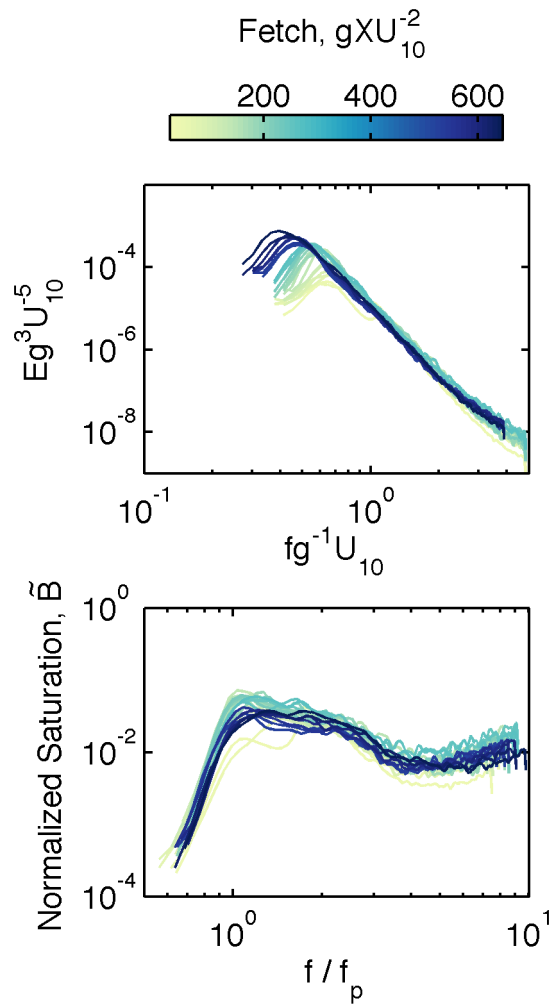where $D(f)$ is an angular spreading function. Here $D(f)$ is used as defined in Gemmrich

Figure 3.2: Top: normalized wave spectral energy density vs. normalized frequency colored by dimensionless fetch for both February 14 ($30 < \hat{x} < 300$) and 15 ($500 < \hat{x} < 600$) data. Bottom: Normalized saturation spectra vs. frequency normalized by peak frequency for both February 14 and 15 data.

et al. (2008). These spectra are shown in Figure 3.2 (bottom). The average of this function, σ_b, over the equilibrium range (we use $f_p \leq f \leq 5f_p$) gives a measure of the mean-square slope of the wave-field. Although the waves from late in the day of February 14th are in the mid-range of the fetch evolution ($200 < \hat{x} < 300$), these waves have the largest saturation levels. The waves of February 15th are more developed ($500 < \hat{x} < 600$), but their mean saturation lies somewhat in the middle of the observed data.

Banner et al. (2002) showed σ_b to exhibit threshold behavior for the onset of breaking and a correlation of σ_b to the breaking rate. Thus, it is expected that other breaking quantities, including b, will relate to σ_b. In this study, some quantities correlate with non-dimensional fetch (non-dimensional wave height, energy, period, frequency, phase and group velocity) while others correlate with saturation (wind speed and stress, wave steepness, wave age, and breaking statistics).

3.3   Evolution of the Distribution of Breaking Crests, $\Lambda(c)$

The calculated $\Lambda(c)$ and $\rho g^{-1} c^5 \Lambda(c)$ distributions are shown in Figure 3.3 using both dimensional and normalized speed. The distributions are unimodal, consistent with the studies of Gemmrich et al. (2008), Thomson et al. (2009), and Kleiss and Melville (2010), and in contrast with Melville and Matusov (2002). Normalizing by the peak phase speed, c_p, shows that the peaks in $\Lambda(c)$ are aligned around $0.5c_p$, with some slight scatter. There is a general trend of increasing breaking with higher mean saturation, consistent with Banner et al. (2002). This trend is also shown in Figure 3.4 (left), where the breaking rate from $\Lambda(c)$ is compared to σ_b. The breaking rate also shows a positive correlation when compared to peak steepness, $H_s k_p / 2$, in Figure 3.4 (right).

Since the breaking dissipation is related to the integral of $c^5 \Lambda(c)$, the distribution of this quantity reveals the contribution to the dissipation from whitecaps at each speed. The curves of Figure 3.3 show that dissipation is dominated by the small amount of breaking at high speeds. This is an important point in the later discussion of microbreakers, which are excluded from measurement when using video methods (see Section 5). Because high-speed noise is amplified by multiplication by c^5, many of these integrals appear unbounded, and it can be difficult to determine where to end the integration. The sensitivity of the later

analysis to the limits of integration is discussed in further detail in Appendix B. A practical upper limit of the point where $\Lambda(c)$ drops below 5% of the peak is used here, which is shown by the transition from solid to dash lines in Figure 3.3. Integrated quantities in the next section use only the solid lines.
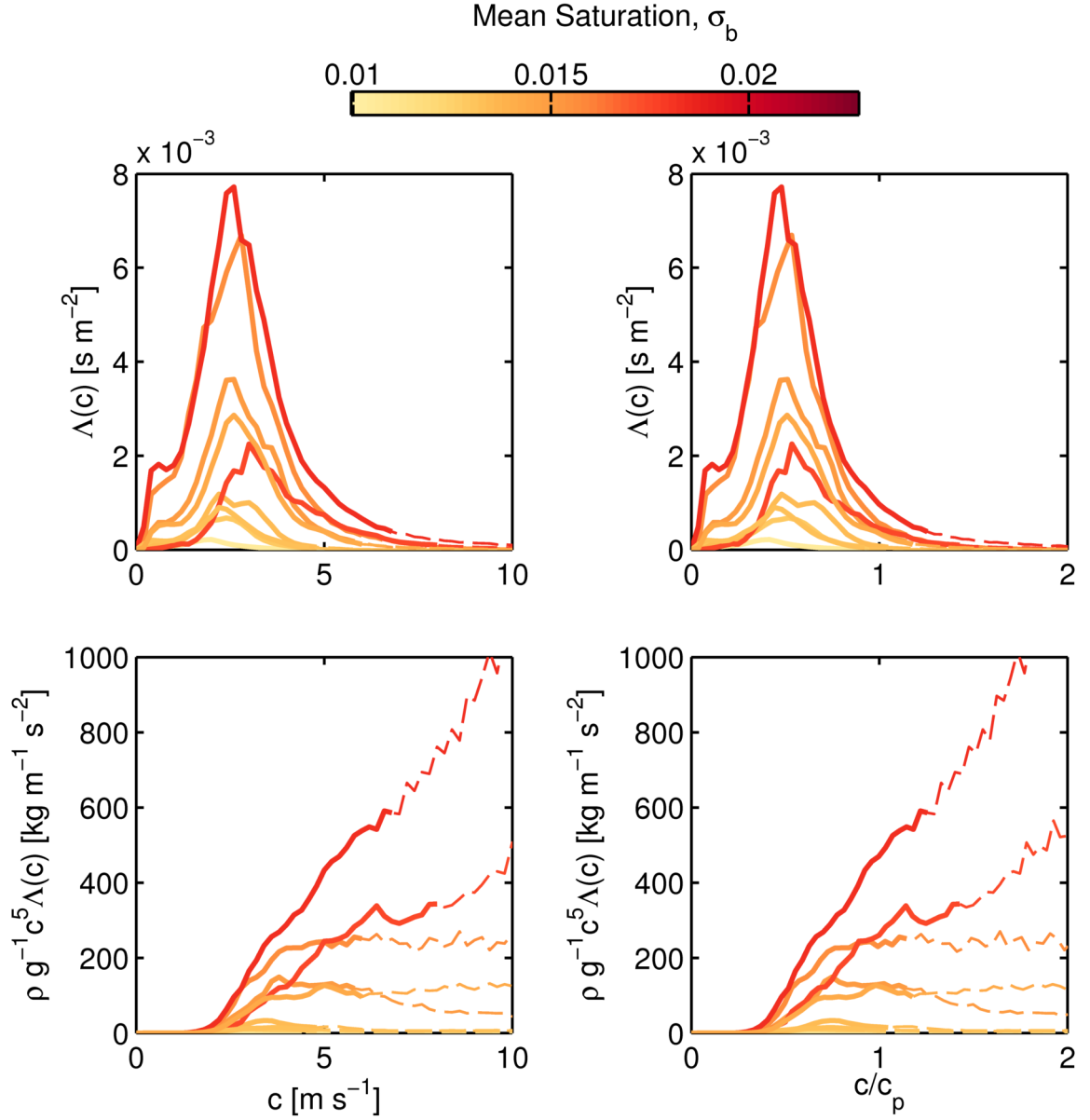
Figure 3.3: $\Lambda(c)$ (top) and $\rho g^{-1} c^5 \Lambda(c)$ (bottom) vs. dimensional (left) and non-dimensional (right) speed. All curves colored by mean normalized saturation. Solid lines indicate the limits of integration for bulk quantities, dotted lines are the continuation of the curve above the upper limit of integration.

Figure 3.4: Breaking rate vs. mean normalized saturation (left) and peak steepness (right) for SWIFT 1 (red) and SWIFT 2 (cyan) for data from February 14th (circles) and February 15th (squares).

Chapter 4

ANALYSIS

4.1   Radiative Transfer Equation

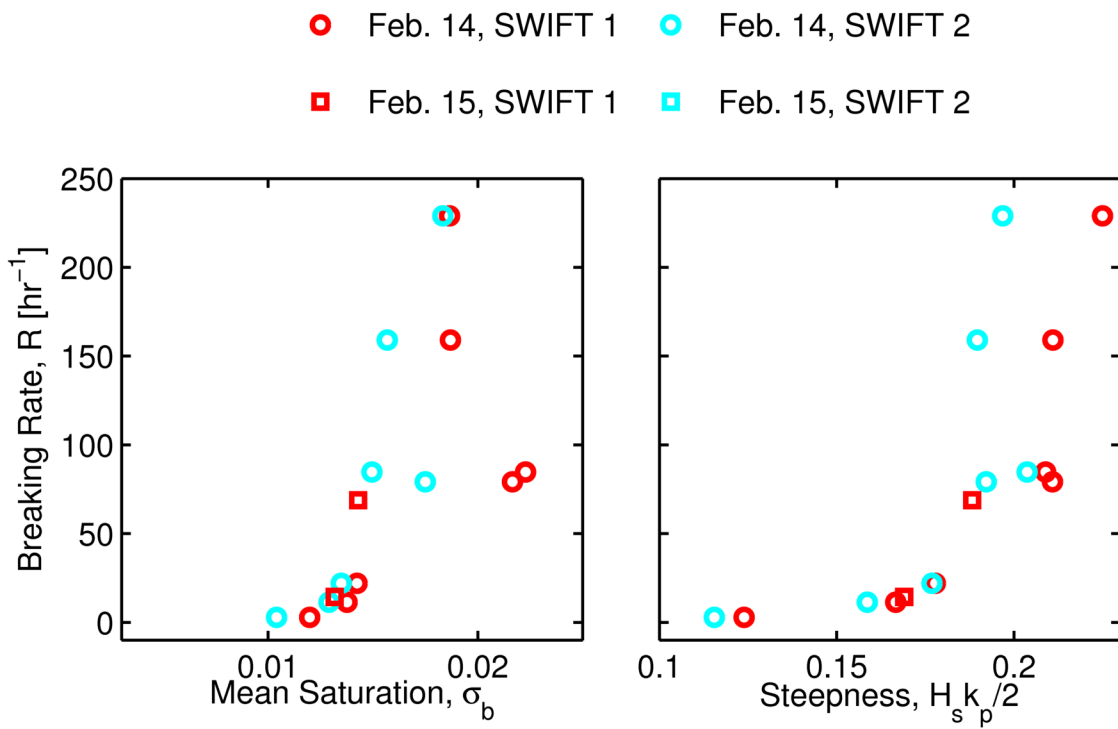The evolution of the ocean surface waves is governed by the Radiative Transfer Equation. This is often stated spectrally, where nonlinear energy transfers between frequencies are explicitly modeled, but for our purposes only the bulk, or spectrally-integrated, energy is considered. Thus the equation reduces to simply

$$\frac{\partial E}{\partial t} + c_g \cdot \nabla E = S_{wind} - S_{brk} \tag{4.1}$$

where S_{wind} and S_{brk} are the energy input from wind and energy lost to breaking, respectively. We attempt to calculate each of these terms to close the energy budget of these fetch-limited waves, and to assess the estimates of wave-breaking dissipation.

A stationary wavefield is assumed, such that $\partial E/\partial t = 0$ and all wave growth is due to advection of wave energy at the group velocity. This approximation is justified by the success of empirical fetch laws when normalized by a constant windspeed, as in Figure 3.1, and by simple scaling of the unsteady term as wave energy over storm onset time $\Delta E/\Delta t \sim 10^{-3}$ Wm^{-2}, which is 2 to 3 orders of magnitude smaller than the other terms in Equation 4.1. There is, however, some variability of the wind that may contaminate the remaining terms.

The calculation of spatial gradient of wave energy is inherently noisy due to the 5-minute estimates of wave spectra. To combat this issue, measurements are first averaged over 500-meter spatial bins. In addition, the gradient is calculated by regressing a line through the origin (assuming no wave energy at zero fetch) and each 500-meter bin. This larger-scale method smooths the otherwise noisy gradient. The group velocity, c_g, is estimated every 500 meters from the peak waves using the deep water dispersion relation. The resulting estimate of $c_g \cdot \nabla E$ is shown in the middle panel of Figure 4.1.

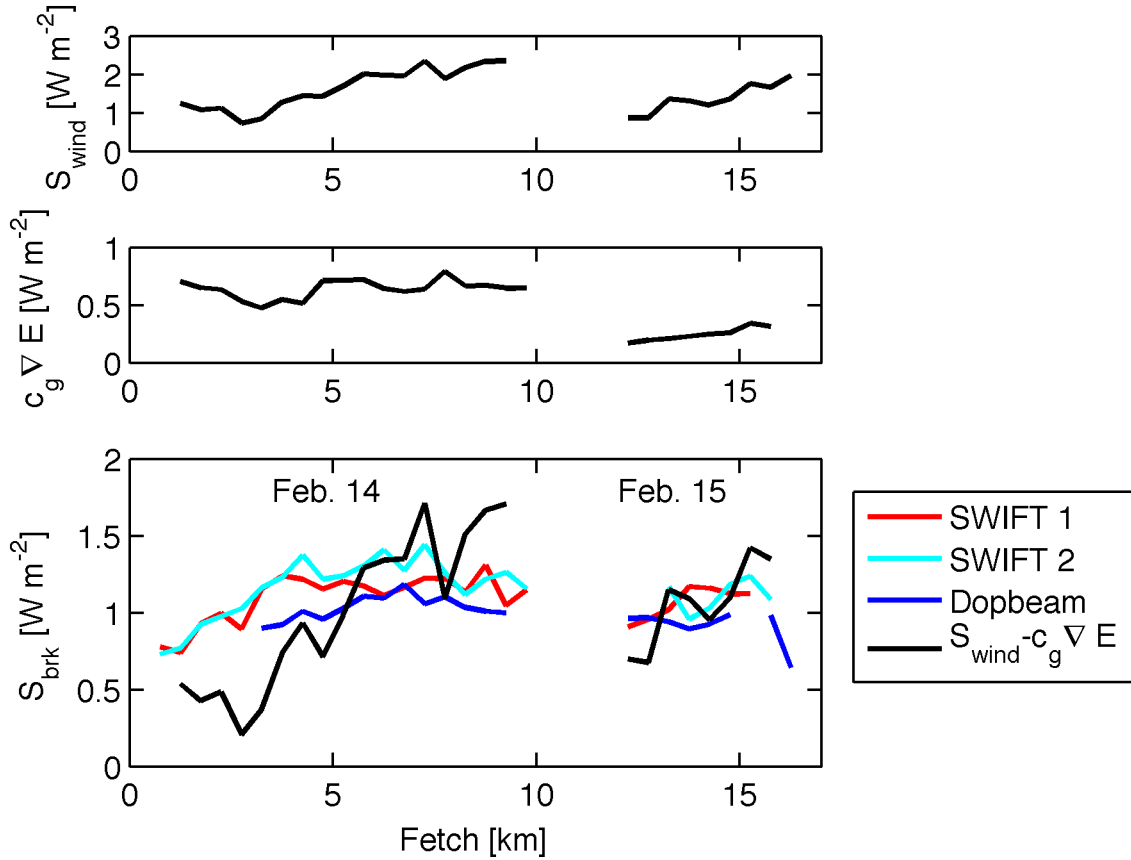The wind input function is parameterized using the wind stress, $\rho_a u_*^2$, and an effective

Figure 4.1: Wind input (top), advective energy flux divergence (middle), and breaking dissipation (bottom) vs. fetch. Dissipation is calculated directly from turbulence for SWIFT 1 (red), SWIFT 2 (cyan), and Dopbeam (blue), and by the residual of the top two panels (black). All quantities are 500-meter averages.

phase speed, c_{eff}, such that

$$S_{wind} = \rho_a c_{eff} u_*^2, \tag{4.2}$$

as described in Gemmrich et al. (1994). There is significant uncertainty in the choice of c_{eff}. Terray et al. (1996) found c_{eff} to be somewhat less than the peak phase speed and show a dependence on wave age, but with much scatter. Here, the best agreement when comparing with *in situ* turbulent dissipation (next paragraph) is found using a daily c_{eff} equal to the minimum phase speed (4.5 and 4.9 ms^{-1} for February 14th and 15th, respectively). The friction velocity, u_*, is calculated from the shipboard sonic anemometer using the inertial dissipation technique. The resulting wind input is shown in the top panel of Figure 4.1.

There are three direct *in situ* measures of the breaking loss, $S_{brk} = \dot{E}$ (from Equation 1.21), from the two SWIFTS and the Dopbeam, and there is a fourth indirect measure of the energy dissipation from the residual of the other RTE terms, $S_{brk} = S_{wind} - c_g \cdot \nabla E$. These four estimates of the wave breaking dissipation rate are shown in the bottom panel of Figure 4.1 and are used in the following section to interpret the $\Lambda(c)$ distributions. The dissipation rates are all within 0.4 Wm^{-2} of each other, except for disparities of up to 1.0 Wm^{-2} in the RTE estimate at the beginning and end of February 14th. Although the agreement is coarse, the consistency of these independent estimates is more than sufficient for the subsequent analysis of the breaking parameter b. The RTE solution is shown largely to validate, on an order of magnitude scale, the conclusions from the *in situ* methods.

4.2 Estimation of the Breaking Parameter b

The value of the breaking parameter b is calculated from

$$b = \frac{S_{brk}}{\rho_w g^{-1} \int c^5 \Lambda(c) dc}, \tag{4.3}$$

using each of the four measures of dissipation, S_{brk}. Application to the nine different calculated $\Lambda(c)$ distributions results in total of 36 estimates of b, which are shown as a function of wave age, mean wave saturation, and wave steepness in Figure 4.2. The independent variables use the average of c_p, U_{10}, σ_b, and H_s within a 250 m vicinity of the $\Lambda(c)$ calculation.
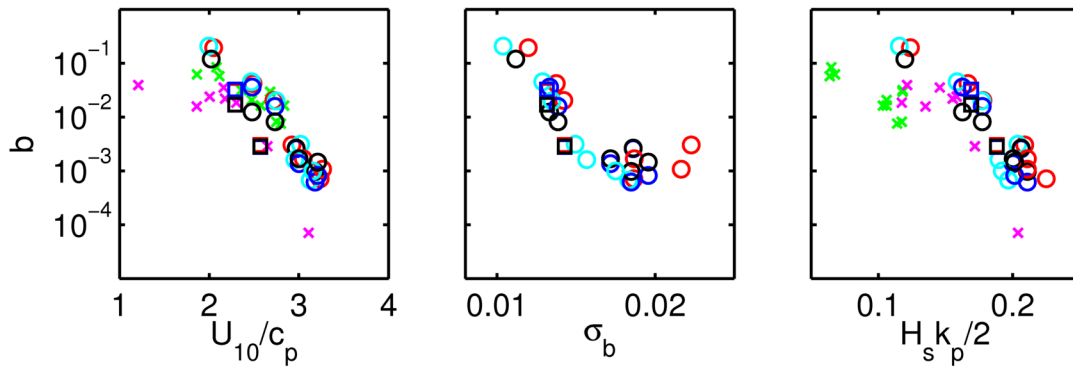
Figure 4.2: Breaking strength parameter, b, plotted against inverse wave age (left), mean normalized saturation (middle), and peak steepness (right). Coloring as in Figure 4.1 and symbols from Figure 3.4, with additional data from Lake Washington in 2006 (green crosses) and Puget Sound in 2008 (magenta crosses).

In addition, we include data taken from measurements made in Lake Washington, WA, in 2006 and Puget Sound, WA, in 2008, originally reported in Thomson et al (2009). Whereas in Thomson et al (2009), a constant b was obtained via regression of $\int c^5 \Lambda(c)dc$ to $\dot{E}_{Dopbeam}$, here individual values of b are calculated. Apart from the updates to the Fourier method detailed in section 2, the $\Lambda(c)$ methodology is similar between the datasets.

Figure 4.2 shows trends of decreasing b with increasing wind forcing (described by inverse wave age, U_{10}/c_p) and increasing wave slope (using mean normalized saturation, σ_b, and peak wave steepness, $H_s k_p/2$). The trends are robust across all dissipation measures and all datasets. The Strait of Juan de Fuca data from early February 14th, as well as the Lake Washington and Puget Sound data, make up the least forced and least steep conditions. The data from late on February 14th contributes the most highly forced and steepest data. The February 15th data lies in the middle of the range from the previous day. Values of b range over three orders of magnitude, which is much larger than the uncertainty in the inputs to Equation 4.3, or the relative error when comparing the four measures of dissipation. The trend in wave age is consistent with the results of Gemmrich et al. (2008). The trend in wave slope contrasts the results of Drazen et al. (2008) and will be addressed in the discussion.

4.3   Comparison with Phillips's Relation

In Figure 4.3, the measured $\Lambda(c)$ are compared with Phillips's predicted function (Equation 1.19). The $\Lambda(c)$ results are plotted in logarithmic coordinates in Figure 4.3 (top), along with a c^{-6} trend line. Due to their peaked shape, the $\Lambda(c)$ functions only approach c^{-6} at the high-speed tail of the distribution, where $c \geq 0.5c_p$. This agreement occurs almost completely outside the equilibrium range, as shown in Figure 4.3 (bottom), where the wave spectra corresponding to these $\Lambda(c)$ have been plotted against phase speed using the dispersion relation. The upper limit of $0.7c_p$ for the equilibrium range was suggested by Kleiss and Melville (2010). They estimated the factors $(4\gamma\beta^3)I(3p)$ from Equation 1.19 to fall in the range of 0.0015–0.0032. Phillips suggested a value of $b = 0.06$ based on the experiments of Duncan (1981). It was shown in the last section, however, that b varies over a wide range in this experiment. In comparing with Equation 1.19 the individual b values found from comparison with *in situ* measurements are used. Thus, if Phillips's formulation, the factors

as estimated by Kleiss and Melville (2010), and the calculated b values are all correct, the $\Lambda(c)$ results should follow the relation:

$$\Lambda(c)bg^{-1}u_*^{-3}c^6 = (4\gamma\beta^3)I(3p) \approx 0.0015 - 0.0032 \tag{4.4}$$

The left-hand side of Equation 4.4 is plotted in Figure 4.3 (middle), with a line at the median proposed value of 0.0024. Within most of the equilibrium range, there is no agreement. However, at high speeds the data flattens and begins to resemble a steady value. The spread between data in this range is around an order of magnitude, and all curves lie somewhat above the proposed $0.0015 - 0.0032$ range.
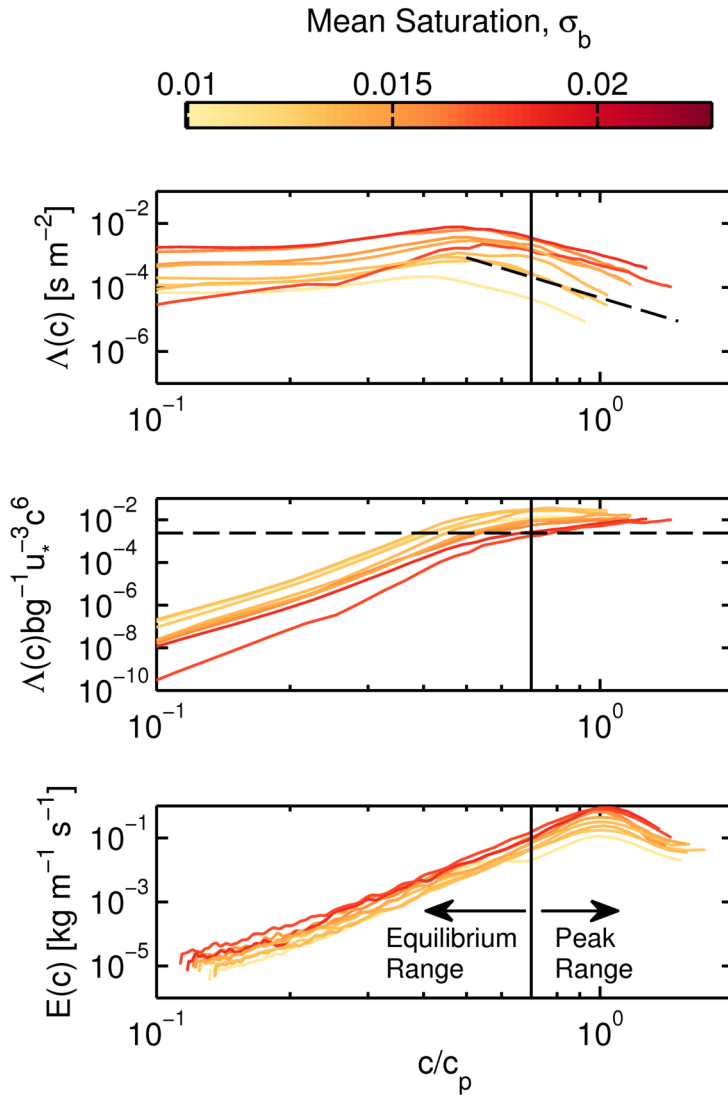
Figure 4.3: $\Lambda(c)$ (top), $\Lambda(c)$ scaled by Phillips's proposed model (middle), and wave energy spectral density (bottom), vs. non-dimensional speed. The dashed line in the top panel shows a c^{-6} tail. The horizontal dashed line in the middle panel is the predicted constant value of scaled $\Lambda(c)$ from Phillips (1985). The vertical solid line in all plots shows the approximate division between the equilibrium range and the peak range.

Chapter 5

DISCUSSION

This study provides a unique quantification of wave breaking dissipation. First, in observing strongly-forced, fetch-limited waves as they develop, a large range of wave conditions are measured under similar winds. In addition, measurements of breaking statistics, *in situ* turbulence measurements, wave spectra, and wind conditions provide a comprehensive description of the breaking dissipation. Analysis of the Radiative Transfer Equation validates the turbulent dissipation measurements as an estimate of the energy lost from waves due to breaking. In addition, breaking data from previous experiments in Lake Washington and Puget Sound are consistent with data from this experiment. The $\Lambda(c)$ results, with peaks centered around $0.5c_p$ are also qualitatively similar to a number of previous field studies of breaking (Gemmrich et al., 2008; Thomson and Jessup, 2009; Kleiss and Melville, 2010). Breaking correlates with steepness and saturation, as predicted by Banner et al. (2002).

The most striking result of this study is that breaking rate varies over a dramatically larger range ($2 \geq R \geq 250$ hr^{-1}) than dissipation rate ($0.2 \geq S_{brk} \geq 1.7$ W m^{-2}). The effect on the resulting b values is seen in Figure 4.2. To reconcile the differing dynamic ranges of $c^5\Lambda(c)$ and S_{brk}, the breaking strength varies over nearly three orders of magnitude. Although both $c^5\Lambda(c)$ and S_{brk} correlate with inverse wave age, mean saturation, and steepness, the breaking strength decreases with these variables as a result of the disproportionate degree of correlation. These trends are robust: changes in processing of $\Lambda(c)$ and S_{brk} result in only minor shifts in the b values relative to their spread (for examples, see Appendices A and B).

This result is critical for interpretation of $\Lambda(c)$ and b. It leads to two potential explanations: Either the nature of breaking changes with wave development, or the c^5 scaling of Equation 1.11 is incomplete. Furthermore, the continued disagreement between observed $\Lambda(c)$ distributions and Phillips's prediction of $\Lambda(c) \sim c^{-6}$ in Equation 4.4 poses additional

questions. We propose that both of these issues are related to a difference in the breaking behavior of waves in the equilibrium range and the peak range, as described below.

5.1 Breaking Strength and Wave Slope

If indeed the nature of breaking is changing with wave development, the trends shown in Figure 4.2 indicate that the relative strength of breaking decreases with increasing wave slope, as measured by mean saturation, σ_b, or steepness, $H_s k_p/2$. This dependence is contrary, however, to the Drazen et al. (2008) result of $b = 0.25 S^{5/2}$, where S is the maximum slope of a focused wave in a laboratory tank. One possible explanation for this difference is that steepness or mean saturation are not representative of breaking wave slope. Even under strong forcing, only a small fraction of the waves in a natural spectrum are breaking. While it seems unlikely that waves would break at smaller slopes in overall steeper conditions, a separate steepness measurement of only breaking waves was not possible in this field study.

A more likely explanation is that natural breakers are not adequately simulated in laboratory studies. Ocean waves break primarily due to modulational instability, whereas laboratory waves are usually induced to break by linear superposition. As noted in Babanin (2011), this difference has already been shown to affect the spectral distribution of dissipation, and may also be the source of the discrepancy between the results presented here and those in Drazen et al. (2008). In addition to wave slope parameters, b is shown to decrease with inverse wave age $U_{10} c_p^{-1}$, as also noted in Gemmrich et al. (2008). Since Drazen et al. (2008) did not investigate breaking with wind forcing, it is possible that this is a stronger dependence, such that the correlation with steepness and saturation is spurious. Other lab/field differences may also be responsible for the deviation. For example, our measured waves are much less steep, $(H_s k_p/2)_{max} \leq 0.28$, than the breakers in Drazen et al. (2008), $S_{min} \geq 0.3$. Finally, three-dimensional wave effects (i.e., the short-crestedness that is a signature of whitecaps) are not well simulated in flume experiments.

5.2 Deviation from Duncan c^5 Scaling

Another possible explanation for the observed trends in b is from deviations in the Duncan scaling of Equation 1.11. This scaling forms the basis for calculating breaking dissipation

from $\Lambda(c)$. The c^5 dependence on speed is partly responsible in this data for the large spread in b, as large c breaking events occur more often in rough conditions and are heavily weighted in the $c^5\Lambda(c)$ distribution (see the bottom plots of Figure 3.3). Deviations from c^5 can be incorporated to the $\Lambda(c)$ dissipation model through a spectral $b(c)$, as opposed to the bulk b used here. This approach would be analogous to that used by Romero et al. (2012) in studying wave breaking in the Gulf of Tehuantepec Experiment (GOTEX). They proposed two spectral models of b,

$$b_1(k) = A_1(B(k)^{1/2} - B_T(k)^{1/2})^{5/2} \tag{5.1}$$

and

$$b_2(k) = A_2(\tilde{B}(k)^{1/2} - \tilde{B}_T(k)^{1/2})^{5/2} \tag{5.2}$$

where $B(k)$ is the spectral saturation in wavenumber, $\tilde{B}(k)$ is the normalized saturation, and A_1, A_2, $B_T(k)$, and $\tilde{B}_T(k)$ are coefficients fit to their data. These models are based on the results of Banner and Pierson (2007) and Drazen et al. (2008) showing a 5/2 power law dependence on wave slope, using the fact that $B(k)$ is related to the mean-square-slope (mss). This formulation in k can be converted to c using the deep water dispersion relation, and thus shown to alter the c^5 dependence of dissipation.

In contrast, we solve for bulk (i.e., non-spectral) values of b and find a negative dependence on wave slope. A bulk b estimate is implicit to the use of *in situ* measurements of dissipation (see Equation 4.3), which, at present, cannot resolve spectral components. The alternative is to infer spectral dissipation from the residual of the spectral Radiative Transfer Equation (as opposed to the integrated version in Equation 4.1), as done in Romero et al. (2012). However, this approach is sensitive to the wind input function, as evident by the three wind models used in Romero et al. (2012).

Although the use of non-spectral *in situ* dissipation measurements is preferred here, comparison with the $b(k)$ results of Romero et al. (2012) is illuminating. Qualitatively, Romero et al. (2012) show three regimes of $b(k)$. For large k, corresponding to phase speeds less than 4.5 m s^{-1}, they calculate unreasonably high breaking strengths which they

attribute to not resolving microbreakers (see Section 5.4). For intermediate k, or speeds roughly between the peak in $\Lambda(c)$ and the dominant phase speed, their b is relatively constant at around 10^{-3}, with slight inflections. For $k < k_p$, their b drops dramatically by a full order of magnitude to around 10^{-4}. Thus, treating our data with the spectral b from Romero et al. (2012) would diminish the effect of the large $c^5\Lambda(c)$ at speeds at and above c_p. This would partially reconcile the large range of breaking activity with the much smaller range of dissipation.

5.3 Peak and Equilibrium Breaking

In introducing $\Lambda(c)$, Phillips (1985) recognized that breaking functioned differently in waves of different scales. Indeed, the formulation behind Equation 4.4 should only be expected to be valid within the equilibrium range. As described by Phillips (1985):

> "Only over wavenumbers that are more distant both from the spectral peak and from the upper limit to this range than half the interval of wavenumbers that is needed to specify these non-local processes, that is, only well inside the equilibrium range, can these scaling arguments be used to represent as, in effect, spectrally local."

Figure 4.3 (bottom) shows the wave spectra plotted against c/c_p, where the equilibrium range is the region of constant positive slope at $c/c_p < 0.7$. There is almost no overlap with the region of c^{-6} observed in the $\Lambda(c)$ distributions (Figure 4.3, top), or the region of $\Lambda(c)bg^{-1}u_*^{-3}c^6$ convergence (Figure 4.3, middle), both of which occur at $c/c_p > 0.7$. Kleiss and Melville (2010) show the same paradox in their Figure 12(a).

The revelation that significant breaking occurs near the spectral peak, especially when weighted by c^5 and contrary to the expectations of Phillips (1985), along with the $b(k)$ results of Romero et al. (2012), points toward a fundamental difference in breaking between peak and equilibrium waves. A bulk b estimate reconciles all of the breaking, on average, from a wavefield with both equilibrium and peak waves, superimposed. The relative contributions from these components can be quantified as the energy ratio $E(3f_p)/E(f_p)$, using three times the peak frequency as an *ad hoc* center for the equilibrium range. As shown in Figure 5.1,
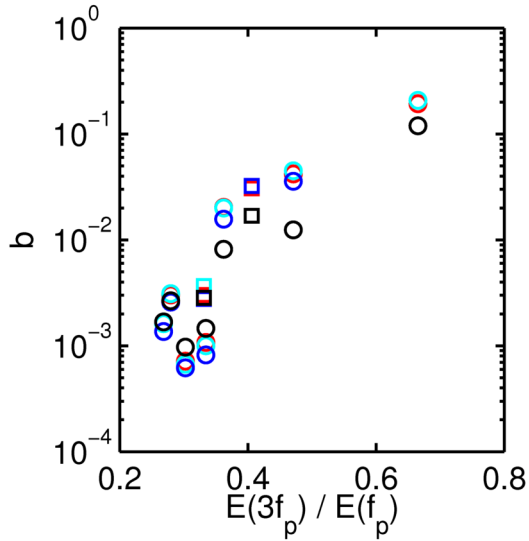
Figure 5.1: Breaking strength parameter, b, plotted against the ratio of energy in the equilibrium range to energy in the peak waves. Colors and symbols as in Figure 4.2.

this ratio is positively correlated with b, suggesting that breaking is stronger in wavefields that have a greater fraction of energy in the equilibrium range. An alternate interpretation of the breaking parameter b is the fraction of energy lost when a wave breaks. A large, steep wave can then dissipate large amounts of energy and still have a small b value, so long as most of the wave persists after the breaking event. This is consistent with the spilling breakers observed for the peak waves in a pure wind sea. For the smaller waves, within the equilibrium range, a greater fraction of the wave may be lost during breaking (or indeed, the entire wave may be lost), and thus the b value would be higher. Resolving these questions requires *in situ* wave-by-wave and spectral measurements of dissipation, as can be achieved in laboratory experiments. These methods are not yet available in the field, however, so this specific hypothesis remains to be tested. For now, it is apparent that the value of b is highly sensitive to contributions to $c^5 \Lambda(c)$ from wave breaking in the peak range and correlates with the relative energy contained in the peak and equilibrium waves.

5.4   Limitations to $\Lambda(c)$

A major limitation of all video observations of wave breaking is the omission of microbreakers, which create turbulence but do not entrain air (and thus do not cause a whitecap). Jessup and Phadnis (2005) measured significant micro-scale breaking in laboratory experiments at winds of 9 m s^{-1} using infrared imaging. In the open ocean, cool skin conditions rarely are favorable enough to make these measurements, especially when large-scale breaking is present. The contribution of wave dissipation from micro-breaking at different sea states continues to be an open question. For the $\Lambda(c)$ distributions calculated in the present study, extrapolation to include microbreakers by requiring c^{-6} for $c/c_p < 0.7$ does not change the main results. The b values are somewhat reduced, but the trends with wave age and wave slope persist.

Another limitation of this study is the lack of directional treatment, $\Lambda(c, \theta)$. This is appropriate for the fetch-limited pure wind sea conditions, however, in other conditions directionality may be important (e.g., Gemmrich et al. 2008). Directionality could not be calculated from this dataset because of the shipboard camera configuration. With a camera height of 7 m and incidences angles of $60° - 70°$, changes in sea surface elevation due to the waves themselves can manifest as movement in the lateral, or y, direction. This corrupts the y-velocities and prevents the calculation of an accurate directional spectrum.

In calculating $\Lambda(c)$, there is some ambiguity in the definition of the breaker speed, c. In Phillips's theory, c refers to the phase speed of the breaking wave. It has been observed, however, that the speed of the whitecap is actually somewhat less than the phase speed. Laboratory experiments (Rapp and Melville, 1990; Banner and Pierson, 2007; Stansell and MacFarlane, 2002), show a linear relationship between the two speeds of the form $c_{brk} = \alpha c_p$, where c_p is the phase speed, c_{brk} is the observed speed of the whitecap, and α ranges from 0.7 to 0.95. Here, we apply $\alpha = 1$, because we have no direct measure of c_{brk}/c_p. Other constant values of α would modulate our results somewhat, but the trends would remain intact. In addition, it has been theorized that the breaking speed of small waves would be enhanced by the orbital motion of dominant long waves. However, both Thomson and Jessup (2009) and Kleiss and Melville (2011) noted that the correction of this effect produces

an overall small change in the results. In the fetch-limited conditions of Juan de Fuca Strait (and lacking significant swell), this effect is neglected.

Finally, it was shown in Kleiss and Melville (2011) that the speed of advancing foam in breaking waves tends to slow over the course of a breaking event. Since the Fourier method includes contributions from speeds throughout the duration of breaking, it distributes the contributions from a single breaking event to a number of speed bins. It has been asserted that this interpretation of breaker speed is contrary to the original definition of the $\Lambda(c)$ function by Phillips (1985) (Mike Banner, personal communication). The uncertainty introduced by slowing crests in the Fourier method is explored in more detail with synthetic data in Appendix A, and is shown not to change the trends in b.

Chapter 6

CONCLUSIONS

Shipboard video observations of breaking waves were made for fetch-limited conditions during two days of a winter storm in the Strait of Juan de Fuca. Video data was processed into $\Lambda(c)$ distributions using the Fourier-based method of Thomson and Jessup (2009) with only minor modifications. Meanwhile, wave-following drifters provided turbulent dissipation measurements of the same seas.

The waves grow and lengthen over the fetch as expected by previously derived empirical relations. $\Lambda(c)$ results show a peaked distribution around speeds somewhat greater than half the peak phase speed. These distributions appear to decrease like c^{-6} as predicted by Phillips (1985), but at speeds outside the equilibrium range. Breaking rates from $\Lambda(c)$ correlate with two bulk measures of wave slope: mean normalized saturation and peak steepness. Indirect estimates of breaking dissipation from the difference of wind energy flux and energy flux divergence validates the turbulent dissipation measurements.

Calculations of the breaking strength parameter, b, are made from comparison of the fifth moment of the $\Lambda(c)$ distributions with the dissipation measurements. The breaking strength is found to decrease with increasing steepness and mean saturation, contrary to laboratory measurements made by Drazen et al. (2008). This could be due to differences between ocean waves and laboratory waves. Another explanation is that there are differences in breaking between wave scales that are not resolved with a bulk b interpretation using a c^5 scaling of dissipation. We speculate that peak waves may lose a smaller fraction of their energy in breaking than equilibrium waves. The breaking strength, b, is shown to correlate with the ratio of energy in the equilibrium range to peak energy.

These trends were observed strictly under narrow-banded, fetch-limited conditions. They remain to be tested in open ocean conditions. In addition, phase-resolved or wave-by-wave dissipation measurements are not yet possible. However, as ocean video observations

continue to become more prevalent and *in situ* methods are improved, it is likely that the relationship between breaking kinematics and dynamics will be further solidified.

BIBLIOGRAPHY

Y. C. Agrawal, E. A. Terray, and M.A. Donelan. Enhanced dissipation of kinetic energy beneath surface waves. *Nature*, 359:219–220, 1992.

A. Anis and J. N. Moum. Surface wave-turbulence interactions: Scaling $\epsilon(z)$ near the sea surface. *J. Phys. Oceanogr.*, 25:2025–2045, 1995.

A. V. Babanin. *Breaking and Dissipation of Ocean Surface Waves*. Cambridge Univ. Press, New York, 2011.

M. L. Banner and O. M. Phillips. On the incipient breaking of small scale waves. *J. Fluid Mech.*, 64:647–656, 1974.

M. L. Banner and W. L. Pierson. Wave breaking onset and strength for two-dimensional deep water wave groups. *J. Fluid Mech.*, 585:93–115, 2007.

M. L. Banner, A. V. Babanin, and I.R. Young. Breaking probability for dominant waves on the sea surface. *J. Phys. Oceanogr.*, 30:3145–3160, 2000.

M. L. Banner, J. R. Gemmrich, and D.M. Farmer. Multiscale measurements of ocean wave breaking probability. *J. Phys. Oceanogr.*, 32:3364–3375, 2002.

CERC. *Shore protection manual*. U.S. Army Coastal Engineering Research Center, 3 volumes edition, 1977.

C. C. Chickadel, R. A. Holman, and M. H. Freilich. An optical technique for the measurement of longshore currents. *Journal of Geophysical Research*, 108(C11):1–17, 2003.

L. Ding and D.M. Farmer. Observations of breaking wave statistics. *J. Phys. Oceanogr.*, 24:1368–1387, 1994.

F. Dobson, W. Perrie, and B. Toulany. On the deep-water fetch laws for wind-generated surface gravity-waves. *Atmosphere-Ocean*, 27:210–236, 1989.

M. Donelan, M. Skafel, H. Graber, P. Liu, D. Schwab, and S. Venkatesh. On the growth-rate of wind-generated waves. *Atmosphere-Ocean*, 30:457–478, 1992.

M.A. Donelan, J. Hamilton, and W. H. Hui. Directional spectra of wind-generated waves. *Phil. Trans R. Soc. Lond. A*, 315(1534):509–562, 1985.

D.A. Drazen, W. K. Melville, and L. Lenain. Inertial scaling of dissipation in unsteady breaking waves. *J. Fluid Mech.*, 611:307–332, 2008.

J. H. Duncan. An experimental investigation of breaking waves produced by a towed hydrofoil. *Proc. R. Soc. London Ser. A*, 377:331–348, 1981.

J. H. Duncan. The breaking and non-breaking wave resistance of a two-dimensional hydrofoil. *J. Fluid Mech.*, 126:507–520, 1983.

J. Gemmrich. Strong turbulence in the wave crest region. *J. Phys. Oceanogr.*, 40:583–595, 2010.

J. R. Gemmrich and D. Farmer. Near-surface turbulence in the presence of breaking waves. *J. Phys. Ocean.*, 34:1067–1086, 2004.

J. R. Gemmrich, M. L. Banner, and C. Garrett. Spectrally resolved energy dissipation rate and momentum flux of breaking waves. *J. Phys. Oceanogr.*, 38:1296–1312, 2008.

J.R. Gemmrich, T.D. Mudge, and V.D. Polonichko. On the energy input from wind to surface waves. *J. Phys. Oceanogr.*, 24:2413–2417, 1994.

K. Hasselmann. On the non-linear energy transfer in a gravity-wave spectrum. part i. general theory. *J. Fluid Mech.*, 12:481–500, 1962.

T. H. C. Herbers, P. F. Jessen, T. T. Janssen, D. B. Colbert, and J. H. MacMahan. Observing ocean surface waves with gps-tracked buoys. *J. Atmos. Ocean. Tech.*, 29:944–959, 2012.

K. Todd Holland, Robert A. Holman, Thomas C. Lippmann, John Stanley, and Nathaniel Plant. Practical use of video imagery in nearshore oceanographic field studies. *IEEE Journal of Oceanic Engineering*, 22:81–92, 1997.

P. A. E. M. Janssen. Quasi-linear theory of wave generation applied to wave forecasting. *J. Phys. Oceanogr.*, 21:1631–1642, 1991.

A. Jessup and K. Phadnis. Measurement of the geometric and kinematic properties of microscale breaking waves from infrared imagery using a PIV algorithm. *Measur. Sci. Tech.*, 16:1961–1969, 2005.

A. Jessup, C. Zappa, and M. Loewen. Infrared remote sensing of breaking waves. *Nature*, 385:52–55, 1997.

S. Kawai, K. Okada, and Y. Toba. Field data support of three-seconds power law and $gu_*\sigma^{-4}$-spectral form for growing wind waves. *J. Oceanogr. Soc. Japan*, 33:137–150, 1977.

S.A. Kitaigorodskii. Contribution to an analysis of the spectra of wind-caused wave action. *Izv. Akad. Nauk SSSR Geophys.*, 9:1221–1228, 1962.

S.A. Kitaigorodskii. On the theory of the equilibrium range in the spectrum of wind-generated gravity waves. *J. Phys. Oceanogr.*, 13:816–827, 1983.

S.A. Kitaigorodskii, M.A. Donelan, J. L. Lumley, and E. A. Terray. Wave turbulence interactions in the upper ocean. part ii. statistical characteristics of wave and turbulent components of the random velocity field in the marine surface layer. *J. Phys. Oceanogr.*, 13:1988–1999, 1983.

J. M. Kleiss and W. K. Melville. Observations of wave breaking kinematics in fetch-limited seas. *J. Phys. Ocean.*, 40:2575–2604, 2010.

J. M. Kleiss and W. K. Melville. The analysis of sea surface imagery for whitecap kinematics. *J. Atmos. Ocean. Tech.*, 28:219–243, 2011.

P. K. Kundu and I. M. Cohen. *Fluid Mechanics (4th Edition)*. Elsevier, 2008.

E. Lamarre and W. K. Melville. Air entrainment and dissipation in breaking waves. *Nature*, 351:469–472, 1991.

M. R. Loewen and W. K. Melville. Microwave backscatter and acoustic radiation from breaking waves. *J. Fluid Mech.*, 224:601–623, 1991.

W. K. Melville. Energy dissipation by breaking waves. *J. Phys. Oceanogr.*, 24:2041–2049, 1994.

W. K. Melville. The role of surface-wave breaking in air-sea interaction. *Annu. Rev. Fluid Mech.*, 28:279–321, 1996.

W. K. Melville and P. Matusov. Distribution of breaking waves at the ocean surface. *Nature*, 417:58–63, 2002.

W. K. Melville and R. J. Rapp. Momentum flux in breaking waves. *Nature*, 317:514–516, 1985.

J. W. Miles. On the generation of surface waves by shear flow. *J. Fluid Mech.*, 3:185–204, 1957.

O. M. Phillips. On the generation of waves by turbulent wind. *J. Fluid Mech.*, 2:417–445, 1957.

O. M. Phillips. The equilibrium range in the spectrum of wind-generated ocean waves. *J. Fluid Mech.*, 4:426–434, 1958.

O. M. Phillips. Spectral and statistical properties of the equilibrium range in wind-generated gravity waves. *J. Fluid Mech.*, 156:495–531, 1985.

O. M. Phillips, F. Posner, and J. Hansen. High range resolution radar measurements of the speed distribution of breaking events in wind-generated ocean waves: Surface impulse and wave energy dissipation rates. *J. Phys. Ocean.*, 31:450–460, 2001.

W. J. Plant. Whitecaps in deep water. *Geophys. Res. Let.*, 39(L16601), 2012.

R. J. Rapp and W. K. Melville. Laboratory measurements of deep-water breaking waves. *Phil. Trans R. Soc. Lond. A*, 331:735–800, 1990.

L. Romero, W. K. Melville, and J. M. Kleiss. Spectral energy dissipation due to surface-wave breaking. *J. Phys. Oceanogr.*, 42:1421–1444, 2012.

R. L. Snyder, F. W. Dobson, J. A. Elliot, and R. B. Long. Array measurements of atmospheric pressure fluctuations above surface gravity waves. *J. Fluid Mech.*, 102:1–59, 1981.

P. Stansell and C. MacFarlane. Experimental investigation of wave breaking criteria based on wave phase speeds. *J. Phys. Oceanogr.*, 32:1269–1283, 2002.

H. V. Sverdrup and W. H. Munk. Wind, sea, and swell: Theory of relation for forecasting. Technical Report Publ. No. 601, Hydrographic Office, U.S. Navy, 1947.

E.A. Terray, M.A. Donelan, Y.C. Agrawal, W.M. Drennan, K.K. Kahma, A.J. Williams, P.A. Hwang, and S.A. Kitaigorodskii. Estimates of kinetic energy dissipation under breaking waves. *J. Phys. Oceanogr.*, 26:792–807, 1996.

J. Thomson. Wave breaking dissipation observed with 'swift' drifters. *J. Atmos. Ocean. Tech.*, in press, 2012.

J. Thomson and A. Jessup. A fourier-based method for the distribution of breaking crests from video observations. *J. Atmos. Ocean. Tech.*, 26:1663–1671, 2009.

J. Thomson, A. Jessup, and J. Gemmrich. Energy dissipation and the spectral distribution of whitecaps. *Geophys. Res. Let.*, 36(L11601), 2009.

Y. Toba. Local balance in the air-sea boundary process, iii. on the spectrum of wind waves. *J. Oceanogr. Soc. Japan*, 29:209–220, 1973.

M.J. Yelland, P.K. Taylor, I.E. Consterdine, and M.H. Smith. The use of the inertial dissipation technique for shipboard wind stress determination. *J. Atmos. Ocean. Tech.*, 11:1093–1108, 1994.

I.R. Young. *Wind Generated Ocean Waves.* Elsevier Ocean Engineering Book Series. Elsevier, New York, 1999.

Appendix A

TIME-VARYING BREAKING CREST SPEED

Synthetic data were created to test the Fourier method for crests that slow during active breaking. This effect was shown in Kleiss and Melville (2011) in their Figure 13, and potentially biases estimates of $\Lambda(c)$ towards lower speeds if the true phase speed of the breaking component is the maximum speed of the whitecap (i.e. at the onset of breaking). The synthetic data is a binary time series resembling thresholded, natural, crests.[1] The breaking crests follow a normal distribution centered around 4 m/s. They also vary in crest length, duration, and direction.

Because the speed and crest length of the synthetic breakers is prescribed, the true $\Lambda(c)$ distribution is easily calculated and compared with the curve obtained from the Fourier method. Synthetic breaking crests were initially kept at a constant speed throughout their duration. This control case is shown in Figure A.1 (left). In the next artificial experiment, crests were made to slow down similar to the data of Kleiss and Melville (2011). Their speed decreased linearly through their duration to 55% of their original speed. Figure A.1 (right) shows a comparison of the $\Lambda(c)$ distributions from the maximum crest speed, average crest speed, time-varying crest speed (similar to the "elemental method" of Kleiss and Melville, 2011), and the Fourier method. As expected, distributions from all other methods are centered on lower speeds than the maximum speed curve. The Fourier method actually resembles the true curve from averaging individual crests speeds more than the time-varying distribution.

The error in $\Lambda(c)$ between the Fourier and true maximum speed methods is calculated at each c, and an average error is calculated as weighted by the true maximum $\Lambda(c)$. This

---

[1]When "perfect" crests (i.e. straight lines of one pixel width) were examined, the Fourier method showed significant aliasing from high frequency components due to Gibbs phenomenon. Crests were then given some randomness in speed along the crest length to make the Fourier transform more well-behaved. In even the best natural data there is plenty of noise present to achieve this effect.
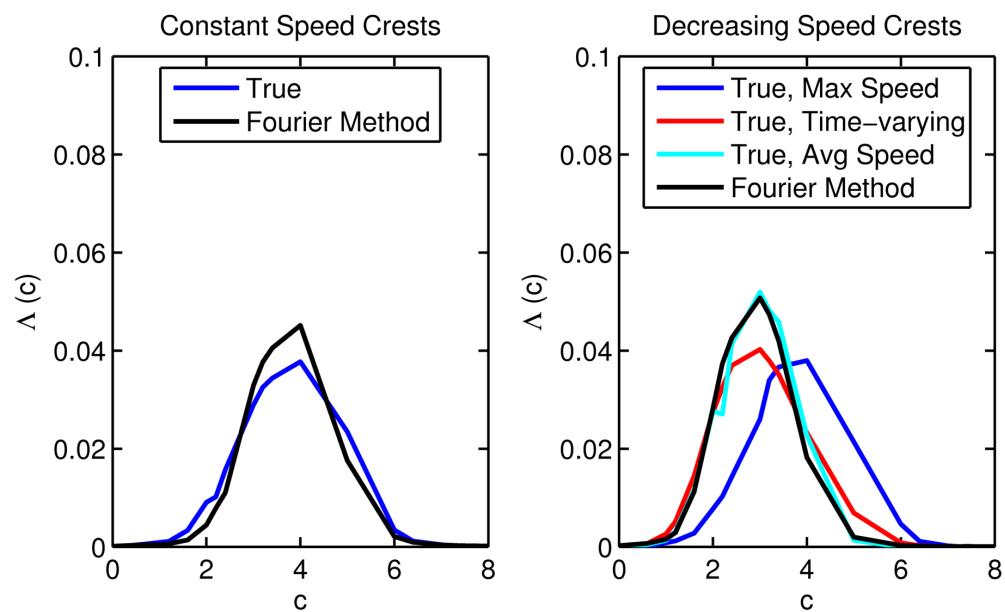
Figure A.1: Comparison of the true $\Lambda(c)$ distribution with the estimate from the Fourier method for synthetic data. Left: Crests propagating at a constant speed, true distribution is shown in blue and Fourier method estimate is black. Right: Crests slowing over their duration as in Kleiss and Melville (2011). True $\Lambda(c)$ distributions based on the maximum crest speed is blue, from the time-varying crest speed is red, from the average crest speed is cyan, and Fourier method estimate is black.
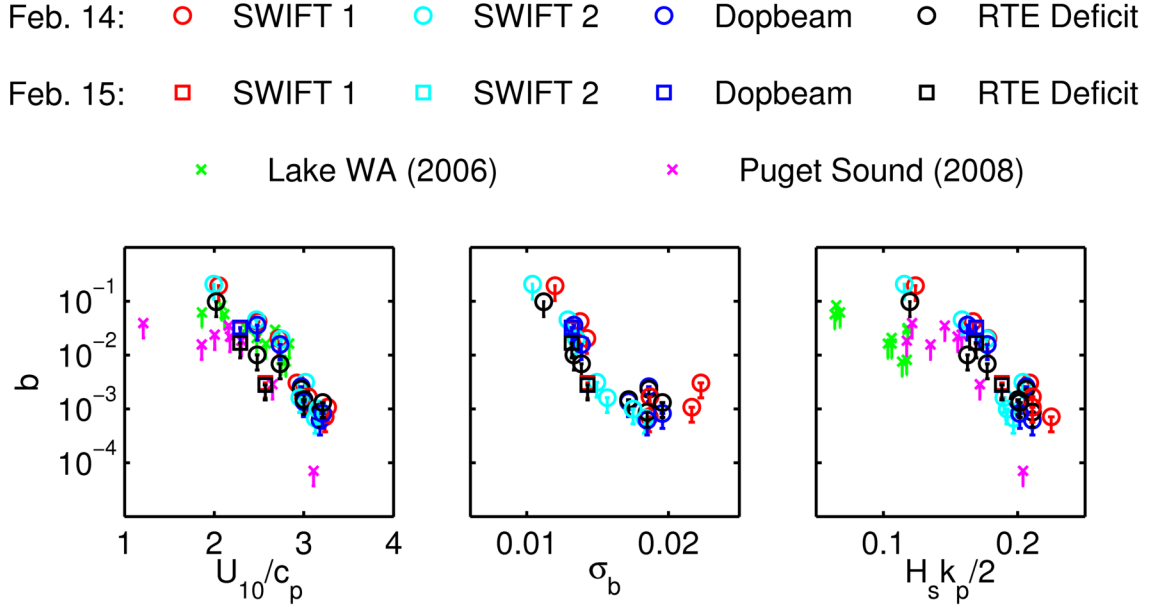
Figure A.2: Breaking strength parameter, b, with error bars from synthetic data of time-varying crest speed, plotted against inverse wave age (left), mean normalized saturation (middle), and peak steepness (right). Colors and symbols as in Figure 4.2. Error bars are calculated using the estimated positive bias of 90% in the Fourier method.

average error is 88% of the true maximum $\Lambda(c)$. Additionally, a bias is propagated through in the calculations of a breaking strength, b, from Equation 4.3 using an arbitrary constant value for $S_{brk}g\rho^{-1}$. The Fourier method was found to bias b high by 90%. With this percent bias, it is possible to place bars on the plots of b from the experimental data, as shown in Figure A.2. Even with this seemingly large difference based on interpretation of crest speed, the error bars are minuscule compared with the scatter of the data and the large range over which the trends are exhibited. Moreover, if the bias is consistent over all data points, the b values would be slightly altered but the trend should be unchanged.

Appendix B

SENSITIVITY TO LIMITS OF INTEGRATION

The calculation of b depends on the total dissipation from integration of $c^5 \Lambda(c)$ over all speeds of breaking. However, the factor of c^5 presents a signal-to-noise problem. Even small contributions to $\Lambda(c)$ at large speeds can add significantly to the total dissipation. This is a common problem, as seen in the $c^5 \Lambda(c)$ distributions of Gemmrich et al. (2008) and Kleiss and Melville (2010). Even Phillips's theoretical relation for $\Lambda(c)$ (Equation 4.4) is prone to this issue, as the resulting integrand has a c^{-1} shape, the improper integral of which does not converge. In time-domain methods such as Gemmrich et al. (2008) and Kleiss and Melville (2010), the upper limit of integration can be infinite because no breaking is calculated above certain speeds. The problem is exacerbated when using the Fourier method, however, as $\Lambda(c)$ never approaches zero due to noise in the spectrum. No clear solution presents itself, so instead the sensitivity of the resulting b values to the upper limit of integration is examined.

$\Lambda(c)$ can be transformed to a function of the number of pixels moving at each speed. This presents a physically intuitive way to define the noise floor. For example, the upper limit of integration can be defined as the point when $\Lambda(c)$ falls below 1 pixel per speed bin ($dc = 0.2$ ms^{-1}). Figure B.1 shows the trends in b, similar to Figure 4.2 (using SWIFT dissipation only for clarity), with error bars corresponding to the range of b from changing the limiting value from 1 pixel to 100 pixels. Large error bars indicate that the value of b is highly sensitive to the integration cut-off. The largest range occurs for the largest value of b (least total breaking) and for the smallest value of b (most breaking at high speeds). The cut-off at 5% of the peak $\Lambda(c)$, shown by the symbols, pulls these two uncertain values nearer the rest of the b values. Therefore, the uncertainty in these b values only makes the trends in wave age, mean saturation, and steepness more stark.
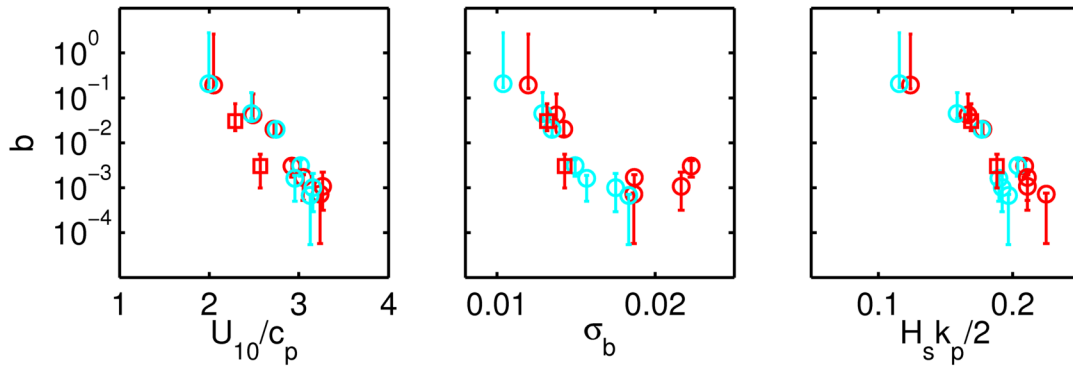
Figure B.1: Breaking strength parameter, b, with error bars from varying upper limit in integration of $c^5 \Lambda(c)$, plotted against inverse wave age (left), mean normalized saturation (middle), and peak steepness (right). Colors and symbols as in Figure 4.2 (SWIFTs 1 and 2, only). Error bars are calculated from varying the upper limit of integration from a limiting value of 1 to 100 equivalent pixels per speed bin.